Numerical and experimental study on the parametric roll resonance for a fishing vessel with and without forward speed

Isar Ghamari[*,a], Marilena Greco[a,b,c], Odd M. Faltinsen[a,b], Claudio Lugni[b,c]

[a] *Department of Marine Technology, Norwegian University of Science and Technology (NTNU), Trondheim, NO-7491, Norway*
[b] *Centre for Autonomous Marine Operations and Systems (AMOS), NTNU, Trondheim, NO-7491, Norway*
[c] *CNR-INM, Institute of Marine Engineering, Rome, Italy*

ABSTRACT

The parametric resonance in roll motion (known shortly as parametric roll) was studied for a fishing vessel in regular waves. This is an instability and resonance phenomenon that can lead the roll to reach very high oscillation amplitudes at its natural frequency, depending on the damping level involved. In the worst cases it is responsible for vessel capsize. Here the problem was investigated numerically and experimentally, performing dedicated physical tests on a typical Norwegian fishing vessel with blunt hull and small length-to-beam ratio.

Experimentally, a dedicated study was carried out on the SFH112 fishing vessel in scale 1:10 in regular head-sea waves with different wave frequencies and steepnesses. The tests were performed without and with forward speed, with corresponding Froude number Fn = 0.09 and 0.18. Numerically, a blended method was developed based on a 6-DOF 3D hybrid method where the radiation and diffraction potentials were computed for zero forward speed by WAMIT and used in the STF strip theory to obtain speed dependent loads. The convolution integrals were used to account for the effect of radiation free-surface memory effect. Nonlinearities in the Froude-Krylov and restoring loads were accounted for by integrating the corresponding pressure terms on the instantaneous wetted-hull surface defined by the incident waves and body motions. Use of the weak-scatterer hypothesis in radiation and diffraction loads has also been considered. The method was applied to reproduce and complement the experiments on the SFH112 fishing vessel. The numerical simulations showed good agreement with the experimental results. For the cases near the instability border of a 1-DOF Mathieu-type instability diagram, the physical and numerical predictions were different in terms of parametric roll occurrence. The instability borders for the experimental cases are also different from the instability borders of 1-DOF Mathieu-type instability diagram. The instability region for the experiments and 6DOF simulations cover a wider range of frequency ratio and the threshold value of metacentric height variation amplitude to have parametric roll seems to be lower than predicted by the 1-DOF Mathieu instability diagram. The results also show that the instability region for the cases with forward speed shifts to the lower frequency ratios(natural roll frequency to encounter frequency ratio) compared to the cases without forward speed. The effect of the weak-scatterer hypothesis on the results is also assessed and shown to be important for parametric roll. The results show that the simulations without this hypothesis tend to underestimate the occurrence and severity of parametric roll especially in longer and steeper waves.

1. Introduction

Parametric roll (PR) resonance was not considered as a serious technical issue for naval architects and maritime researchers until several incidents occurred during the past two decades. In October 1998, the *M/V APL China* (a C11 class post-Panamax container ship with 260 m length and 40 m breadth) was travelling from Kaohsiung, Taiwan, to Seattle, USA, carrying around 4000 containers. Off Alaska's

Aleutian Islands, she was overtaken by a severe storm lasting more than 12 hours. Besides the violent storm, very large motions during the worst part of the storm made the situation even more critical. Significant heave and pitch amplitudes in addition to a roll angle around 35–40 degrees made this incident one of the biggest in its type in the history. The following day, the damage was quantified: One fourth of the 1300 on-deck containers were lost overboard and almost similar amount was severely damaged [1] and the ship itself suffered structural damage [2].

This is said to be the biggest cargo disaster in history, in which the total lost cargo worth over USD 100 millions [3],which is even more than the total value of the ship (USD 50 millions)[2]. This incident amongst some others, put the parametric rolling in hot spot for researchers in naval architecture and hydrodynamics.

Dunwoody [4,5] showed a relation between the astern incident wave spectra and the metacentric height spectra and then found that the variation of metacentric height has the same effect as reducing the roll damping and then he tried to find the roll stability limits in this process.

Parametric rolling might build up very fast to high roll angles and might even lead to capsizing of the ship. As a try to understand and explain the basic mechanisms of ship capsizing, some researches tried to study the problem with simplified theoretical and numerical models (Umeda et al.[6], Sanchez et al. [7], Oh et al.[8]). Hamamoto and Panjaitan [9] did an analytical study of the ship capsize phenomenon for a container ship due to parametric rolling to identify the limits of critical conditions in this regard. Munif and Umeda [10] used a 6-DOF non-linear mathematical model to study the parametric roll and capsizing limits for a ship in astern sea and successfully validated the results against experiments for a container ship. They found that the effect of heave and pitch might be negligible in low steepness waves while it is important in steep waves.

Initially most of the researches thought that parametric rolling occurred in the following-sea waves but gradually some works started to analyse the occurrence of parametric rolling in head-sea waves as well. Perez and Sanguinetti [11] did some experiments regarding the parametric rolling in longitudinal seas for small fishing vessels with different stern sections. They showed that a transom stern can amplify the roll motions more than the presence of a round stern. They also concluded that since this phenomenon can make the ship reach a very high roll angle in a very short time, the crew of the ship also should be aware of this latent threat.

Neves et al. [12] studied, numerically and experimentally, the dynamic stability of two small fishing vessels in head sea. They compared the vulnerability of two types of stern to parametric excitation and concluded that a transom and wide stern is more prone to go into the unstable zone than a round stern.

Neves [13] studied the motions of a fishing vessel using a 3-DOF (heave, roll and pitch) model and using the Taylor series expansion of up to second order for the restoring loads. This model showed a tendency to overestimate the roll motion in the unstable zones. Neves and Rodriguez [14] continued the previous work but using the Taylor series expansion for coupled restoring loads up to the third order, which showed a better agreement with experimental data.

After the APL China incident in 1998, several incidents involving parametric roll in head-sea waves were reported such as: destroyers incidents (Francescutto [15]), Maersk Carolina ship incident in January 2001, RoPax ships (Francescutto et al., [16]) and PCTC vessels (Palmquist and Nygren, [17]). So an increasing attention was given to head-sea parametric roll occurrence. Francescutto et al. [16] investigated, numerically and experimentally, the conditions for parametric rolling with discussion on the threshold value for the roll damping to avoid parametric roll and for the wave excitation to trigger parametric roll. They also examined the parametric-roll amplitude once the instability is excited. Spyrou [18] reviewed the state-of-the-art regarding the parametric roll for a deterministic and probabilistic environment and presented some new ideas about the development of practical design criteria. The work by Francescutto (2004) and Spyrou (2005) made the foundation for the ITTC recommended procedure and guidelines for predicting the occurrence and magnitude of parametric roll [19].

Levadou et al. [20], studied the parametric roll problem in different loadings and wave heading (head and bow seas) conditions and as a function of ship speed. They documented several polar diagrams with the steady-state roll amplitude against varying speed and headings for a given wave period. Many graphs are presented for different wave periods and these diagrams can be used as operational guidance for helping the ship masters in order to avoid extreme roll motions. Shin et al. [21] discussed the technical background of the American Bureau of Shipping (ABS) Guide for the assessment of parametric roll resonance in the design of container ships. They verified the susceptibility and severity criteria in the mentioned report using a series of numerical simulations and finally concluded that both susceptibility and severity criteria were verified and showed to be reasonable and reliable. They examined nine ships and checked the criteria against the numerical simulation results and showed that the criteria predicted correctly the presence or absence of the parametric roll in all ships. They also highlighted that in order to obtain reliable results in irregular seas, one realization is not enough and the distribution of parametric roll resonance might not be Gaussian.

Silva et al. [22], studied the parametric roll of a container ship in regular and irregular waves using a partly non-linear strip theory formulation. They used a frequency domain 5-DOF (all motions except surge) system and a roll damping coefficient from the decay tests. The results and comparison with experiments show that this method gives reasonable results for parametric resonance. They also suggested the need for some revision to the IMO's "Guidance to the Master for Avoiding Dangerous Situations in Following and Quartering Seas". Levadou et al. [23], studied the main dimensions, hull form and appendages configuration effects on parametric roll while keeping the draft, metacentric height (GM) and natural roll period constant. They used a relatively simple one degree of freedom non-linear model along with model tests and concluded that, for the C11 container ship, the aft body shape is more important than the bow flare in parametric roll occurrence. They also mentioned that a V-shape aft body is preferable to a U-shape aft body for avoiding parametric roll. McCue et al. [24] also studied the effect of topside shape on parametric rolling for a destroyer in longitudinal seas. Spyrou et al. [25] systematically investigated a post-Panamax container ship rolling, on the basis of several analytical formulas that exist in the industrial guidelines and that are evaluated by a step-by-step process against various numerical predictions. The identification of the instability boundary and the prediction of steady amplitude of roll oscillations were also assessed in their work.

Belenkey et al. [26] presented a background for parametric roll risk analysis of a ship operating in head seas. The ship motions are studied numerically in irregular waves with the conclusion that despite large amplitude motions, pitch and heave retain their ergodic qualities and normal character of distribution while the roll motion clearly is not ergodic and is not necessarily a Gaussian stochastic process. If the statistical properties of a random process could be deducted from a single and sufficiently long random sample, the process is ergodic, otherwise it is not. Bulian et al. [27] presented the preliminary results regarding the problem of non-ergodicity of parametric roll in longitudinal irregular long-crested waves. Some numerical simulations using an analytical 1.5-DOF were performed and showed the effect of ship speed and sea spectrum shape on parametric roll. In the 1.5-DOF simulations, they considered the effect of heave and pitch motions in the metacentric variation.

The alternative to a 6-DOF system for studying parametric roll, is to consider fewer-DOF systems like 3-DOF or 1.5-DOF, where some coupling terms and some degrees of freedom are assumed to be zero in order to simplify the problem while maintaining, hopefully, the relevant terms. In a 1.5-DOF model, for instance, the roll restoring moment is a function of time and roll angle, and should be calculated a priori. Bulian et al. [28], proposed a 1.5-DOF analytical and numerical system for parametric rolling analysis in regular and irregular head seas where heave and pitch motions were considered as quasi-static. They used this model as a tool to find the instability threshold and the roll amplitude above a certain threshold. They validated their model against experimental results of a RoRo ship in both regular and irregular waves.

Greco et al. [29] examined numerically and experimentally the

parametric roll of a fishing vessel in head sea with possibility of bottom slamming and water on deck by using a 3D domain decomposition strategy. Ghamari et al. [30] investigated the parametric roll of a C11 class post-Panamax container carrier ship with and without forward speed using strip theory. They validated the results with some experimental data from literature and showed that, for this ship, the used strip theory method could capture most of the experimental cases. Ghamari et al. [31] and Ghamari [32] studied the parametric roll of a fishing vessel in cases with zero forward speed and also cases with anti roll tanks. The present paper is a continuation of those work with the analysis of cases with forward speed.

In this paper, a blended time domain numerical seakeeping solver is applied for studying parametric instability, its occurrence and features in a fishing vessel. The so-called hybrid method is used to solve the radiation and diffraction problems in cases with forward speed based on the solutions of cases without forward speed from a 3D linear potential-flow solver (like WAMIT). Nonlinearities in the Froude-Krylov and restoring loads were accounted for by integrating the corresponding pressure terms on the instantaneous wetted-hull surface defined by the incident waves and body motions. The effect of using the weak-scatterer assumption in modifying the radiation and diffraction loads is also modelled and studied. Some dedicated new sets of experiments are performed to study this phenomenon in a fishing vessel with and without forward speed to examine the effect of forward motion. They are used also to validate the proposed solution strategy, which in return supports and complements the physical investigation. The experimental data could be a valuable benchmark for validating different numerical simulations. The fishing vessel model and the experiments are outlined in the next section while the numerical solver is described in Section 3. The experimental and numerical results are presented in Section 4. Then the main results are summarized and the conclusions are drawn.

2. Experiments

A comprehensive experimental investigation on the parametric rolling of a fishing vessel was carried out at the CNR-INSEAN basin No. 2. The dimensions of this basin are: *length* x *width* x *depth* = 220m x 9m x 3.6m. The wave basin is equipped with a flap wave-maker, hinged at a height of 1.8 m from the bottom. The experiments were performed on a scaled model (1:10) of a medium sized Norwegian fishing vessel (SFH112). Bilge keels, skeg and anti-roll tank have been used in the experiments. Here we only present the data for experiments with the skeg. The body plan with skeg of the C2575 model and the GZ curve in calm water and also in waves are shown in Figs. 1 and 2, respectively, while Table 1 reports the main particulars. The GZ curve in waves, accounts for the incident wave along the ship and also considers the effects from the heave and the pitch motions. One should note that the case shown in Fig. 2 is related to a case with a steep wave which makes large vertical motions. So it also affects the submerged part and consequently the GM value. One non-common qualitative tendency that was observed, is that the GZ at the wave-crest amidship is larger than that at the wave-trough amidship for heel angle below 21 degrees. This has happened due to the peculiar transom shape with small draft, which gets dry in some conditions and with large vertical motions as in the selected case.

For a better understanding, the snapshots of the model in calm water and in wave, with crest or trough midship, are shown in Fig. 3. As it can be seen in this figure, the transom has a small draft. It means that some metacentric-height contributions from the waterplane area are lost and therefore the GM value decreases for such situations. As it can be seen in Fig. 2, the righting arm is linear for small heel angles (Up to 10˚) while it gets non-linear for larger heel angles.

Fishing vessels in Norway tend to become wider in order to increase the payload due to regulatory length limitations, so the SFH112 vessel is also fairly wide. The midship region of the vessel lacks the uniform sections seen on larger vessels and the body plan shows that the hull
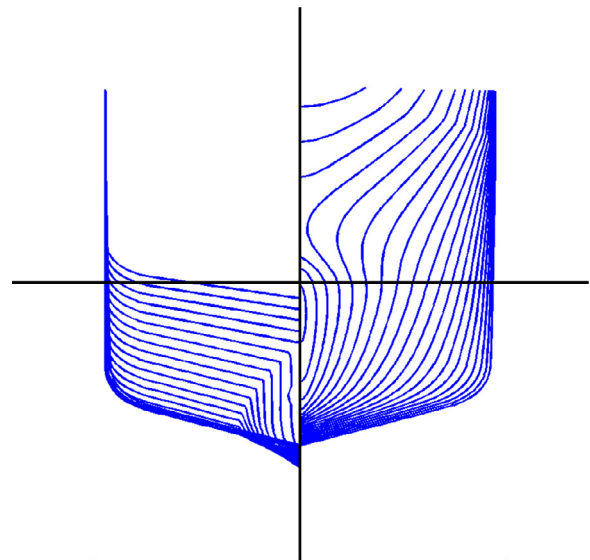

Fig. 1. SFH112 fishing vessel body plan.

portion with similarly shaped sections is small. Besides, the sectional draft is small in the aft part with the consequence that this part may easily get out of the water in waves. This makes the vessel more vulnerable to parametric roll due to larger variation of the water-plane area in waves with wavelengths in the order of the ship length.

The model is placed in the middle of the tank for cases without forward speed. The incident waves are measured by a pair of sensors (capacitance wire probe and finger probe) placed 16 m ahead of the model. The rigid motions of the hull are measured with an inertial (MOTAN) and an optical (Krypton) system. The non-intrusive system Krypton gives the real-time measure of the rigid body motions: 3 CCD cameras detect the position of a reference system fixed to the body and identified through three infrared LEDs. This system enables tracking at a high spatial resolution of less than 1mm for the linear displacements and less than 0.05˚ for the rotational degrees of freedom. The MOTAN is an inertial platform, which measures the accelerations and the angular velocities of a rigid model.

Numerical integration could recover the motion of the body in post-processing with an error around 1mm for the linear displacements and 0.15˚ for the rotational degrees of freedom [33].

In order to limit the mean horizontal motions (mean surge, sway and yaw) of the model, a mooring system of four elastic cables in a symmetrical configuration with respect to the longitudinal hull axis (V-shaped configuration) was placed at the water-plane level and fixed to the carriage. Four load cells were attached between the carriage and the ends of the four cables to measure the pretension (T_0) and the changes in the cable tension during the experiments. Preliminary free-decay tests were performed in calm water and zero forward speed to estimate the damping in the different rigid degrees of freedom. The cases examined here are presented next. The actual incident wave parameters, the damping coefficients and cable tensions from the physical tests are reported and have been used as input in the numerical simulations.

2.1. Uncertainty analysis: repeatability error

In this section, an error analysis is presented to give a global estimation of the maximum error expected for each quantity. Only the repeatability error is estimated. An accurate estimation of this requires the test to be repeated several times, which is time consuming and unlikely to be performed for each test condition. A single physical condition, corresponding to the nominal parameters of wave frequency ratio 0.51 and wave steepness ($k\zeta_a$) 0.10 and $Fn = 0$, is selected. The test is repeated 4 times and each run lasts for at least 30 cycles after the
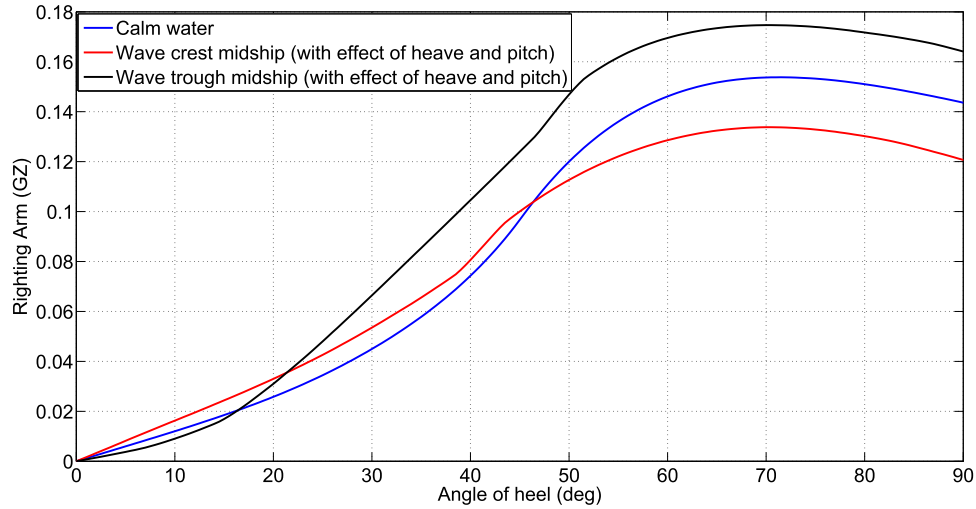
Fig. 2. GZ-curve of the SFH112 fishing vessel in calm water and in waves (corresponding to case C483 with head sea waves, $T_w = 1.43$s, $\zeta_a = 0.107$m).

Table 1
Main particulars of the model scale of the SFH112 fishing vessel in scale 1:10.

Length $L \equiv L_{pp}$	2.95m
Beam B	0.95m
Draft D	0.4m
Freeboard FB	0.477m
Displacement ∇	657.3kg
Block Coefficient C_B	0.58
Longitudinal Center of Gravity (LCG) from AP (Aft Perpendicular)	1.412m
Verical Center of Gravity (VCG) above keel (KG)	0.43m
Transverse metacentric height GM_T	0.07m
Roll Radius of Gyration k_{xx}	0.378B
Pitch and Yaw Radius of Gyration k_{yy}, k_{zz}	0.28L
Natural roll period, T_{n4}	2.97s

steady-state regime has been reached (test cases C489, C494, C498, C501). The parametric roll occurred in all cases with roll steady state value of 15.4˚, 15.25˚, 15.01˚ and 15.24˚, respectively. The error analysis of the heave, roll and pitch motions is performed in this section.

Assuming that the variable for which we want to perform the uncertainty analysis is constant in time (for instance, the mean added resistance in waves, R_{aw}), this would involve the estimate of the average and standard deviation of the variable over N repeated tests, as follows:

$$\bar{R}_{aw} = \frac{1}{N} \sum_{i=1}^{N} R_{aw,i} \tag{1}$$

$$S_{R_{aw}} = \sqrt{\frac{1}{N-1} \sum_{i=1}^{N} (R_{aw,i} - \bar{R}_{aw})^2} \tag{2}$$

In contrast, the uncertainty of the time history of the oscillatory quantities, e.g. the incident wave profile and hull motions, requires the following procedure as described in [33], when assuming regular incident waves and nearly steady-state conditions:

- For each run the steady-state signal is divided into at least 10 temporal windows, each one long two incident-wave periods;
- The mean value on each window is subtracted;
- At each time instant of the time window, the mean and the standard deviation, accounting for the samples coming from all the windows, are estimated.

In this procedure, the windowing process has a small uncertainty estimated to be approximately two time steps in the data acquisition (i.e. approximately 0.0036 s here). For the examined wave case, based

on the first couple of wave transducers ahead of the ship, the expected wave period is 1.518s. This period corresponds to the mean period calculated from the repeatability analysis. The mean time history of the heave, roll and pitch motions together with the error bar giving the standard deviation of the measurements, are shown in Figs. 4–6.

For the cases considered, the mean standard deviations associated with the heave, roll and pitch motions are approximately 1.62%, 0.3% and 0.3% of the motion amplitudes, respectively. This process is not an appropriate process for the incident wave profiles. The wave profile is affected by unavoidable seiching modes of the basin, which are very long standing waves connected with tank resonance and make the signal less repeatable. These seiching modes do not influence the ship motions so much. Since the seiching modes are associated with low frequencies, they do not influence the first harmonics of the incident waves. So we did the FFT analysis of the incident wave profile for the four repetitions and estimated the mean and standard deviation for the first harmonic of the actual incident waves. Since we only used the first harmonic of the waves in the simulations and the first harmonics are the main components for the low steepness waves (the nominal wave steepness here is 0.10), the mean and standard deviation are calculated for them only. For the examined wave case, the mean wave amplitude is 43.83mm and the standard deviation is 2.1% of this mean value. The mean frequency for this harmonic is 0.6588Hz, corresponding to a period of about 1.518s, with a standard deviation as 0.02% of the mean value.

2.2. Studied cases

The tests were performed in head-sea regular waves in the vicinity of parametric resonance instability area. However it should be noted that the instability area is calculated based on a single degree-of-freedom and Mathieu instability diagram. As we know, the parametric resonance based on the 1-DOF formulation occurs when the natural roll frequency (ω_{n4}) is about half of the encounter frequency (ω_e), depending on the roll damping. So these tests were performed varying the frequency ratio $\frac{\omega_{n4}}{\omega_e}$ from 0.46 to 0.54 (ω_{n4} refers to natural frequency in roll in calm water, i.e. it is estimated from the free-decay test at zero-forward speed and no incident waves). The other condition for occurrence of parametric roll is that the waves should be sufficiently high to trigger large changes in the roll restoring. So the wave steepness, $k\zeta_a$, was varied between 0.1 and 0.25. Here, k is the wave number. The experiments performed at Fn = 0, 0.09 and 0.18 are shown in Table 2, 3 and 4, respectively. Since the prescribed incident waves and the actual waves generated in the basin might be a bit different due to experimental errors, we performed FFT (Fast Fourier Transform) of the
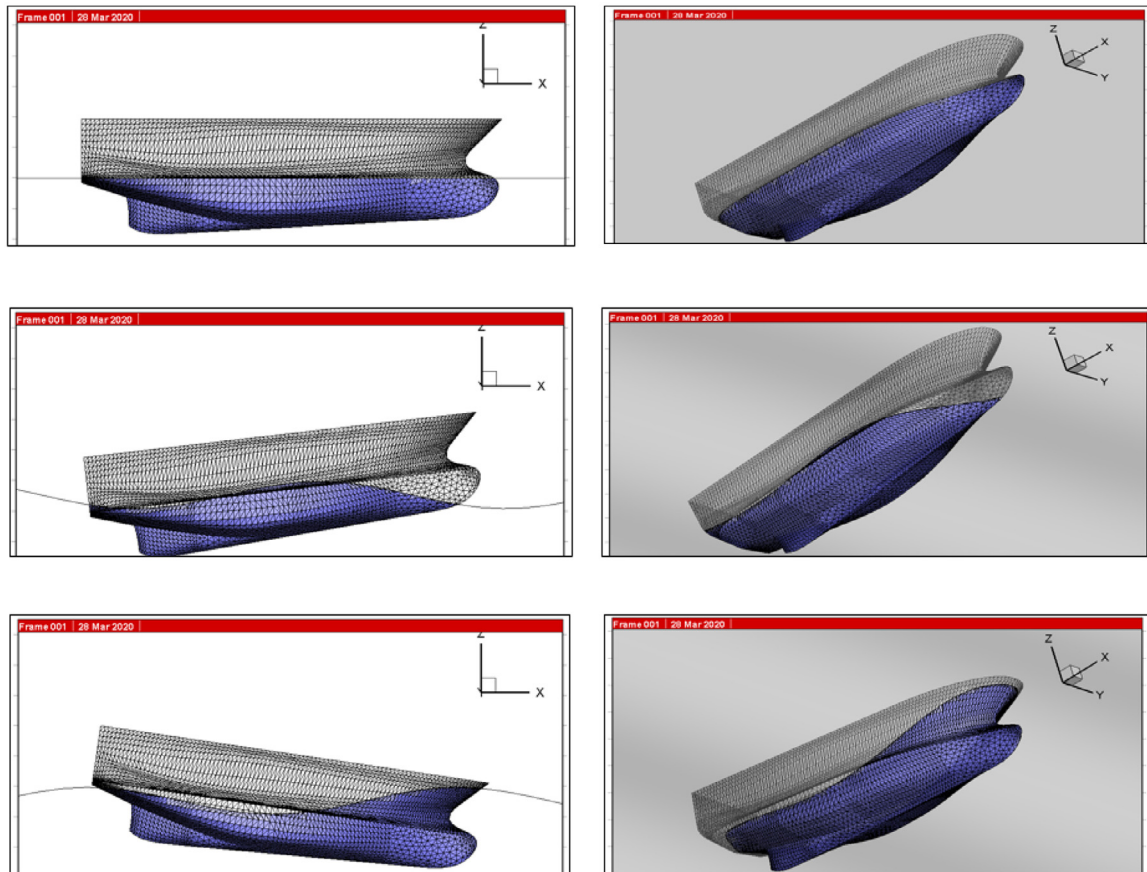
Fig. 3. The incident wave along the ship and the submerged part of the model considering the heave and pitch motions. Top: model in calm water. Middle: wave-crest midship situation. Bottom: wave-trough midship situation. (corresponding to case C483 with head sea waves, $T_w = 1.43$s, $\zeta_a = 0.107$m).

actual incident waves in the experiments for a more accurate estimate of their parameters. The FFT was applied to a time interval of 10 oscillation periods of the wave-elevation evolution measured far upstream of the vessel. Such time interval was selected after the initial transient phase and before the start of relevant ship motions, to ensure nearly steady-state conditions with limited wave reflection effects. Fig. 7 shows a sample result of this FFT procedure for test case C457. The nominal and actual incident-waves for Fn = 0, 0.09 and 0.18 are given, respectively, in Table 2, 3 and 4. The linear incident-wave parameters

identified by the FFT procedure were used as input for the second-order model of the incident waves in the numerical simulations.

By checking the experimental videos for cases with Fn = 0.18, it was clearly observed that the model had a negative small sinkage (rising up) and a small trim angle (bow up) at this forward speed. From the analysis of selected snapshots, a sinkage of 8mm (upward) and a trim angle of 0.5° (bow up) were identified as a rough estimation and included in the numerical simulations at this Froude number.
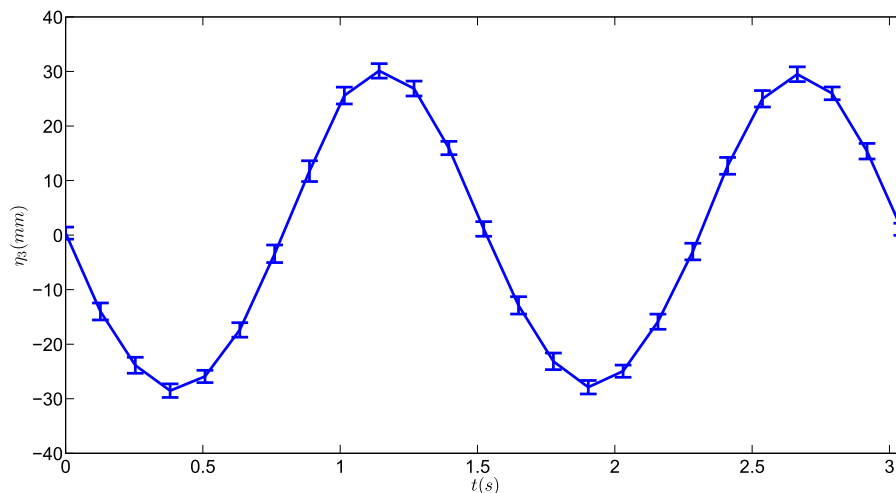

Fig. 4. Repeatability analysis for the case with nominal wave frequency ratio $\frac{\omega_{n4}}{\omega_e} = 0.51$ and wave steepness $k\zeta_a = 0.10$; mean time history of the heave motion together with the error bar ($\pm$ two times of the standard deviation).
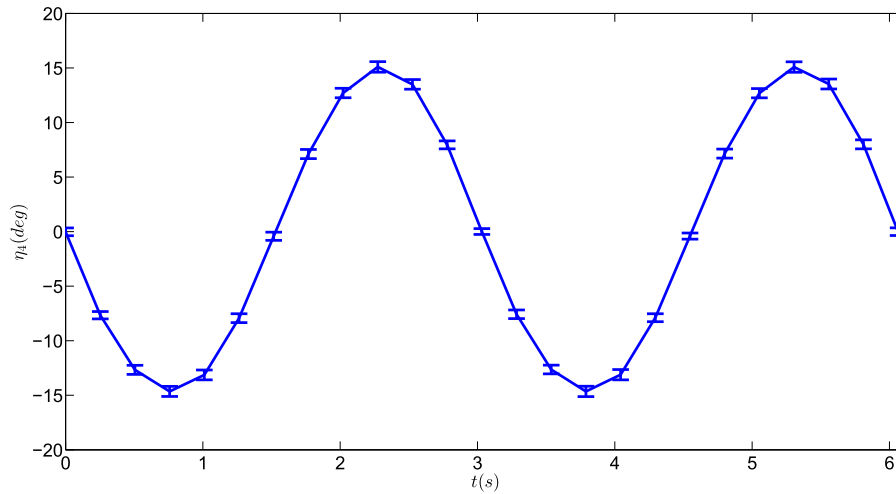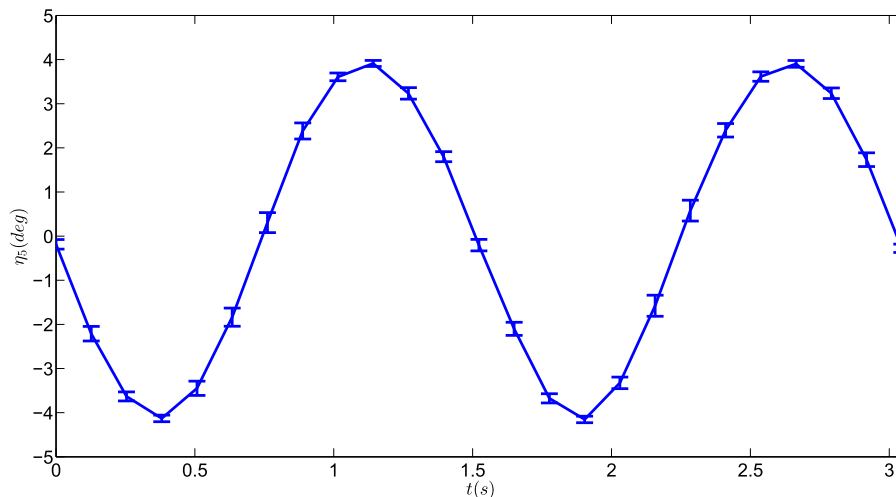
Fig. 5. Repeatability analysis for the case with nominal wave frequency ratio $\frac{\omega_{n4}}{\omega_e} = 0.51$ and wave steepness $k\zeta_a = 0.10$; mean time history of the roll motion together with the error bar ($\pm$ two times of the standard deviation).

2.3. Cable tensions and damping from the tests

The values used in the experiments for the cable angles are $\alpha_f = 25°$ and $\alpha_a = 45°$, as shown in the sketch of Fig. 8. Based on practical experience, it is more efficient for limiting the horizontal motion to have the SB-E part as steel rigid part (shown in black in Fig. 8) and other parts as elastic cables (shown in blue in Fig. 8). In the aft part of the body, the elastic cables are instead directly attached to the ship hull. The coordinates of the attachment points in the body frame coordinate system in calm water are listed in Table 5.

Using the measured tensions, the positions of cables attachment points to the ship model and to the carriage, and the vessel rigid motions in time we can remove the known pretension and plot the (dynamic) cable tension $T - T_p(N)$ versus the cable length variation Δl and identify, by best fitting, the analytical link $T - T_p = f(\Delta l)$ in the form:

$$
T - T_p
= \begin{cases}
T^{min} & \text{if } \Delta l < \Delta l_0 \\
f(\Delta l) = a_0 + a_1 \Delta l + a_2 \Delta l^2 + a_3 \Delta l^3 + a_4 \Delta l^4 & \text{if } \Delta l_0 < \Delta l < \Delta l_1 \\
g(\Delta l) = b_0 + b_1 \Delta l & \text{if } \Delta l > \Delta l_1
\end{cases}
\tag{3}
$$

The application of Eq. (3) leads to a behavior of the dynamic tension as shown in Fig. 9. An example of this dynamic tension identification is given in Fig. 10 for the starboard-side cables in the surge-decay case 451. The tension laws identified from the tests have been used to model the cables in the numerical simulations. They are reported in Table 6. For the cases at Fn = 0.18, there were two sets of cables and consequently two sets of tension laws. One set was for the test case C545 and the second set was for all other cases at this Froude number.

Because the pretension measurement at the aft-port side was not available, in the simulations we used only the tension measurements from the cables on the starboard side and assumed left-right symmetry of the cables.

The free-decay tests in surge, sway, roll and yaw were analyzed using a 1-DOF model and the linear and quadratic damping coefficients were identified. They are given in Table 7 and were used in the simulations.

3. The numerical method

Here, a numerical time-domain blended method is used, based on the Cummins's [34] formulation for the equations of motions in non steady-state conditions. This involves potential-flow radiation loads as sum of instantaneous high-frequency added-mass and damping loads and convolution integrals for memory-effect loads. Strictly speaking

Fig. 6. Repeatability analysis for the case with nominal wave frequency ratio $\frac{\omega_{n4}}{\omega_e} = 0.51$ and wave steepness $k\zeta_a = 0.10$; mean time history of the pitch motion together with the error bar ($\pm$ two times of the standard deviation).

Table 2

Test cases at $Fn = 0$. The frequency ratio $\frac{\omega_{n4}}{\omega_e}$ and the wave steepness $k\zeta_a$ refer to the prescribed incident waves. In each cell, three elements are given vertically, as follows: the first label indicates the case number, the second value is the wave period in seconds and the last value is the actual incident-wave steepness. A cell with only X indicates that the corresponding test was not performed.

$k\zeta_a \downarrow, \frac{\omega_{n4}}{\omega_e} \rightarrow$	0.46	0.47	0.48	0.49	0.50	0.51	0.52	0.53	0.54
0.1	X	X	C459 1.432 0.091	C479 1.461 0.098	C457 1.483 0.096	C501 1.518 0.094	C468 1.550 0.093	C480 1.571 0.107	X
0.15	X	C464 1.404 0.143	C463 1.432 0.143	C462 1.462 0.136	C461 1.491 0.143	C460 1.518 0.137	C469 1.553 0.131	C481 1.578 0.144	C482 1.598 0.154
0.20	C473 1.369 0.197	C472 1.397 0.182	C471 1.426 0.152	C470 1.450 0.198	C466 1.491 0.173	C465 1.510 0.191	C474 1.549 0.188	C484 1.582 0.182	C499 1.595 0.190
0.25	C493 1.387 0.207	C490 1.406 0.214	C483 1.431 0.230	C491 1.465 0.216	C492 1.480 0.229	C495 1.509 0.227	C496 1.538 0.216	C497 1.555 0.241	C500 1.587 0.221

Cummins's approach is valid within linear theory. Researchers have stretched this to the limits including on the right-hand-side of motion equations nonlinear loads and keeping the assumptions of linearity for the radiation and diffraction loads. The same strategy has been used here.

The complete 6-DOF time domain formulation for the body motions in the right-handed inertial reference frame moving with the ship forward speed (where x is positive forward, y is positive to the port side and center of coordinate system lies below center of gravity on the undisturbed free surface) can be written as:

$$\sum_{k=1}^{6} \left[(M_{jk} + A_{jk}(U, \infty))\ddot{\eta}_k + B_{jk}(U, \infty)\dot{\eta}_k + B_{jk}^{quad}|\dot{\eta}_k|\dot{\eta}_k + C_{jk} \right.$$

$$\left. \eta_k + \int_{t-t^*}^{t} K_{jk}(\tau, U)\dot{\eta}_k(t - \tau)d\tau \right]$$

$$= F_j^{Diff} + F_j^{FK,rest} + F_j^{grav} + F_j^{others} \qquad (for \ j = 1,...,6) \tag{4}$$

Here $k = 1, ..., 6$ refers to surge, sway, heave, roll, pitch, yaw motions and their corresponding forces and moments. M_{jk} is the ship mass matrix. $A_{jk}(U, \infty)$ and $B_{jk}(U, \infty)$ are, respectively, the added mass and damping of the ship in case with forward speed U and at infinite frequency. B_{jk}^{quad} is the quadratic viscous damping. $\ddot{\eta}_k$ and $\dot{\eta}_k$ refer to acceleration and velocity, respectively. C_{jk} is the radiation restoring coefficient and K_{jk} is the retardation function. The F_j^{Diff} is the diffraction force, $F_j^{FK,rest}$ is the non-linear Froude-Krylov and hydrostatic restoring force, F_j^{grav} is the ship weight and F_j^{others} are the other forces that might be imposed to the ship, like the cable forces. All of them are expressed in terms of their jth component. The effect of forward speed is considered using a 3D method, which can be found in detail in [32]. The equation system (4) is solved here using a time integration algorithm based on the Runge-Kutta fourth order (RK4) method with constant time step equal to 0.005 times the wave period. The weak-scatterer hypothesis is also used for radiation and diffraction effects modification in time. It can provide a more accurate prediction of motions in long and steeper waves and large body motions. More details about this method is described in the next section. It should be also noted that in the simulations, the linear-wave parameters are needed as input for the second-order wave description used by the numerical method.

3.1. Weak-scatterer hypothesis formulation

In our time domain solver, the radiation-force coefficients and diffraction forces are calculated in the frequency domain before starting the simulations. Based on [35] and [32], the weak-scatterer hypothesis can provide a more accurate prediction of them in long, steeper waves and large body motions. So a modification to the solver formulation is performed as explained here. The main assumption ([35], [36]) is that the incident waves and body motions are large relative to the scattering and radiation wave effects (wavelength-to-ship length ratio sufficiently large). A study on some cases is performed and confirmed that using this hypothesis provides closer results to experiments in terms of parametric roll. The results for this study are explained in Section 5. In this case, the equations of body motions are solved in time in the body-fixed reference frame. In vector form they read [35]:

$$M\ddot{\eta} + \Omega \times M\dot{\eta} + A_\infty \dot{\beta} + \int_0^t K(t - \tau)\beta(\tau)d\tau = F^{FK,rest} + F^{grav} + F^{others}$$

$$\tag{5}$$

where η_i are the six rigid degrees of freedom, Ω is the angular velocity vector $(\dot{\eta}_4, \dot{\eta}_5, \dot{\eta}_6)$ and the upper dots mean the time derivatives along the instantaneous body axes. The cross product of Ω with the first three component of $M\dot{\eta}$ gives the first three components and the remaining give the second three components. A_∞ is the infinite frequency added mass and K is the retardation function. The right-hand-side forces are non-linear Froude-Krylov and restoring loads, ship weight and other

Table 3

Test cases at Fn = 0.09. The frequency ratio $\frac{\omega_{n4}}{\omega_e}$ and the wave steepness $k\zeta_a$ refer to the prescribed incident waves. In each cell, three elements are given vertically, as follows: the first label indicates the case number, the second value is the wave period in seconds and the last value is the actual incident-wave steepness. A cell with only X indicates that the corresponding test was not performed.

$k\zeta_a\downarrow,\frac{\omega_{n4}}{\omega_e}\rightarrow$	0.45	0.46	0.47	0.48	0.49	0.50
0.1	X	X	C521 1.65 0.0976	C538 1.68 0.0972	X	X
0.15	C537 1.59 0.1404	C536 1.62 0.1418	C522 1.65 0.1427	C533 1.68 0.1426	C534 1.71 0.1428	C535 1.74 0.1428
0.20	X	X	X	C539 1.68 0.1838	X	X

external loads including e.g. water-on-deck, slamming, mooring-line and viscous loads, respectively. The incident waves are modeled as second-order Stokes waves. It means that the amplitude of the linear incident wave is needed as input for the simulations. The incident waves and the body motions define the instantaneous wetted-hull surface used for estimating the nonlinear Froude-Krylov and restoring loads and for correcting the linear radiation and scattering loads within the weak-scatterer approximation (see e.g. [37] for details). The latter correction is the reason why the six-component vector β in Eq. (5) is in general different from the body velocity $\dot{\eta}$. One should note that the hydrodynamic potential flow formulation has as a basis an inertial coordinate system formulation and has not been consistently formulated in a body-fixed coordinate system which is an error source in the forward speed dependence of hydrodynamic forces. In our case, the forward speed dependence is based on STF (Salvesen-Tuck-Faltinsen formulation).

The obtained hydrodynamic coefficients are used to estimate the retardation function but within the weak-scatterer approximation, which enforces satisfying the impermeability on the instantaneous wetted hull surface so getting radiation loads as combined with the diffraction loads (through the β_j terms) and in the body-fixed coordinate system. Furthermore, the viscous effects as in the traditional maneuvering analysis by cross-flow formulation are not included, but from the authors experiences, those viscous forces will only matter during maneuvering if the ship makes a tight turn, which is not the case in the present experiments. A simplified model of water on deck and bottom slamming is used in the numerical simulations but for the cases examined here the corresponding loads were small. More details about the assumptions and formulations for these two parts could be found in [35,38] and [33].

3.2. Numerical modeling of the mooring cables

To perform numerical simulations consistently with the experimental investigations, the experimental mooring-line system was modelled as explained in the following. The ship bow is connected to the carriage through a rigid part, $E-SB$, and two elastic cables; while two elastic cables connected directly the stern of the model to the carriage. The numerical modelling of the fore cables is more challenging than that of the aft part, which can be easily estimated once known the instantaneous rigid ship motions. For the fore part, at any time we should find the exact position of joint E and then find the fore-cables length change. A sketch of the cables configuration for a situation with ship-model motions is shown in Fig. 11.

In order to find the exact coordinates of the joint point of the fore

elastic cables and the rigid steel cable, we can solve a system of four equations and four unknowns. The unknowns are the coordinates of the joint point E, (X_E, Y_E, Z_E), and the tension force in the steel part $E-SB$, F_E. The four needed equations are obtained enforcing the equilibrium of the forces acting along EG, EF and $E-SB$ with joint point E and also enforcing the length of the steel part $E-SB$, l_{E-SB}, to be constant and known, i.e.:

$$F_E(X_{SB} - X_E) = -\left[\frac{T_{EG}}{l_{EG}}(X_G - X_E) + \frac{T_{EF}}{l_{EF}}(X_F - X_E)\right] \tag{6}$$

$$F_E(Y_{SB} - Y_E) = -\left[\frac{T_{EG}}{l_{EG}}(Y_G - Y_E) + \frac{T_{EF}}{l_{EF}}(Y_F - Y_E)\right] \tag{7}$$

$$F_E(Z_{SB} - Z_E) = -\left[\frac{T_{EG}}{l_{EG}}(Z_G - Z_E) + \frac{T_{EF}}{l_{EF}}(Z_F - Z_E)\right] \tag{8}$$

$$\sqrt{(X_{SB} - X_E)^2 + (Y_{SB} - Y_E)^2 + (Z_{SB} - Z_E)^2} = l_{E-SB} \tag{9}$$

Here T_{EG}, T_{EF}, l_{EG} and l_{EF} are tension in cable EG, tension in cable EF, cable EG and cable EF length, respectively. The other parameters are points coordinates. One should stress that the tensions T_{EG} and T_{EF} are expressed in terms of the change of their corresponding cable length through Eq. (3) and the latter can be expressed in terms of the coordinates of the involved connection points. For finding the solution of this system of equations, we used the Newton-Raphson method. This method is an iterative numerical method and a criterion should be to discriminate when the equilibrium has been identified. Once the coordinates of the joint point E have been found, the cable forces can be estimated and introduced in the ship equations of motions.

4. Experimental and numerical results

Here the experimental and numerical rigid-ship motions are compared for the different examined cases. The simulations were performed including the weak-scatterer hypothesis. In particular, the first harmonic of the actual incident waves estimated by FFT (see Section 2.2) is used as input in the numerical simulations. The damping coefficients (linear in sway, roll and yaw plus nonlinear roll damping), as shown in Table 7 and identified in the free-decay tests, are used as damping loads at any forward speed and making sure that the linear wave-radiation damping effects are not included twice. To do this, the linear-wave radiation damping coefficient at the natural frequency is subtracted from the linear roll damping coefficient identified from the tests, while the quadratic term is not modified. Similarly, the cable-tension laws identified in the tests were used in the simulations. The roll damping of
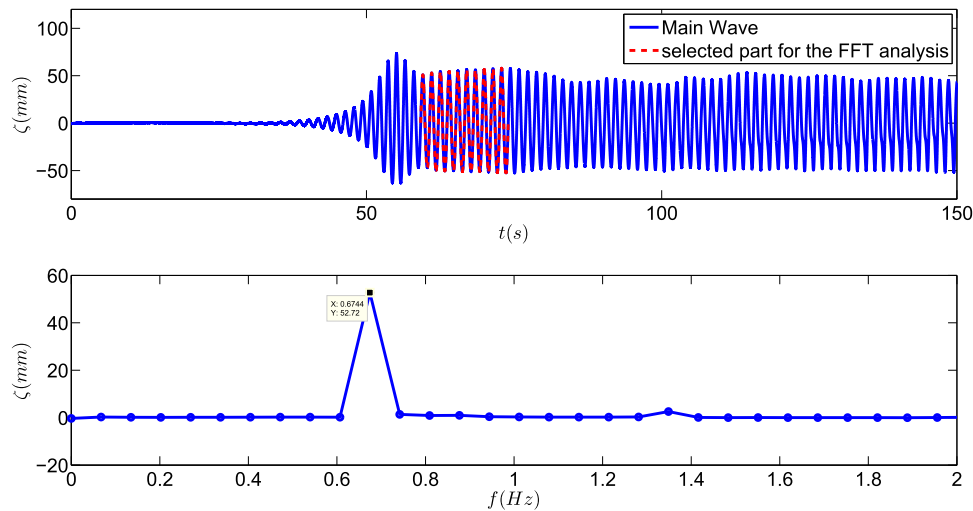
Table 4

Test cases at Fn = 0.18. The frequency ratio $\frac{\omega_{n4}}{\omega_e}$ and the wave steepness $k\zeta_a$ refer to the prescribed incident waves. In each cell, three elements are given vertically, as follows: the first label indicates the case number, the second value is the wave period in seconds and the last value is the actual incident-wave steepness. A cell with only X indicates that the corresponding test was not performed.

$k\zeta_a\downarrow,\frac{\omega_{n4}}{\omega_e}\rightarrow$	0.43	0.44	0.45	0.46	0.47	0.48	0.49	0.50
0.1	X	X	X	X	X	C548 1.88 0.0969	X	X
0.15	C555 1.73 0.1422	C554 1.76 0.1424	C551 1.79 0.1429	C550 1.82 0.1427	C549 1.86 0.1421	C545 1.89 0.1428	C552 1.92 0.1432	C553 1.92 0.1429

Fig. 7. Wave elevation in time for C457 test (top plot) and the FFT analysis of its selected part (bottom plot).

the bare hull and due to the bilge keel and skeg is studied experimentally and numerically with and without forward speed in [39].

4.1. Cases at Fn = 0

The test matrix for the cases without forward speed is shown in Table 2. To assess the proper numerical modelling of the cables, preliminarily the free-decay tests are examined. Fig. 12 presents the experimental and numerical decay in surge (C451 case), showing a good agreement. Similarly, Fig. 13 examines the roll decay (case C450) and confirms a good agreement between physical and numerical results.

Table 8 shows the experimental and numerical results for roll-motion amplitude in nearly steady-state conditions in all studied cases in head-sea regular waves.

In most of the cases the two results are the same in terms of occurrence of PR and the roll amplitudes are also in an acceptable agreement.

As an example, the numerical and experimental results of vessel motions for the case C457 are shown in Fig. 14. This is a case with parametric roll caused by waves with the lowest examined steepness and frequency ratio equal to 0.5. From the figure, the results are in a good agreement (except for the surge). The numerical and experimental cable tensions for case C457 are given in Fig. 15, showing similar behaviours and values. In general, in the examined head-sea waves, the surge motion is characterized by an important negative mean value leading to a drift of the vessel toward the stern. As a result, the fore

Table 5

Coordinates of the cable attachment points to the carriage and to the ship model in the body fixed coordinate system. They are defined in Fig. 8.

Node	x(m)	y(m)	z(m)
F	3.9057	0.82	0.05
G	3.9057	-0.82	0.05
E	2.1287	0.0	0.0
SB	1.8087	0.0	-0.0067
D	-2.379	-0.82	0.05
C	-2.379	0.82	0.05
B	-1.592	0.0	0.025

cables are tensioned and show an oscillatory behaviour, while those in the aft of the vessel experience only the pretension. The experimental cable tensions have a high frequency and quite high amplitude noise though.

The motions in sway and yaw show a disagreement in the comparison, and it might be probably due to the fact that we assume that the cables are initially left-right symmetric in the simulations while it is not exactly like that in the experiments. Besides, the reflection of waves from the tank walls in the experiments might be important. On the other hand, one should note that both of these motions are quite small when compared to other rigid degrees of freedom. The transient phase of surge motions is also a bit different between experiments and numerical simulations, which is consistent with the differences observed in Fig. 15 for the fore cable tensions.
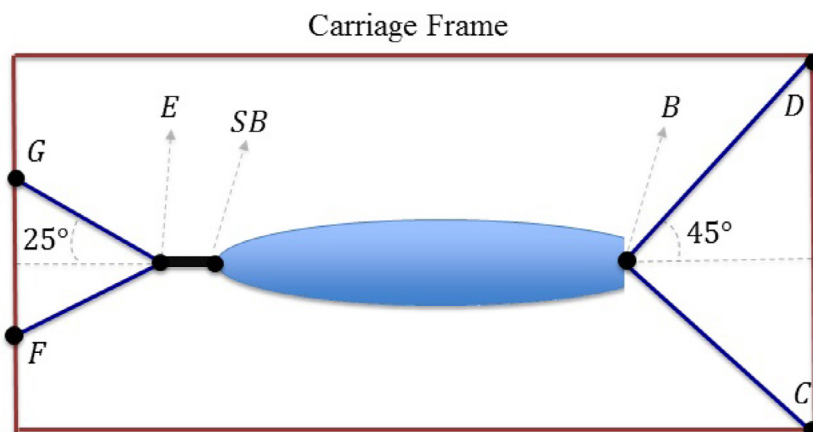

Fig. 8. Top view of the experimental cable configuration in calm water.
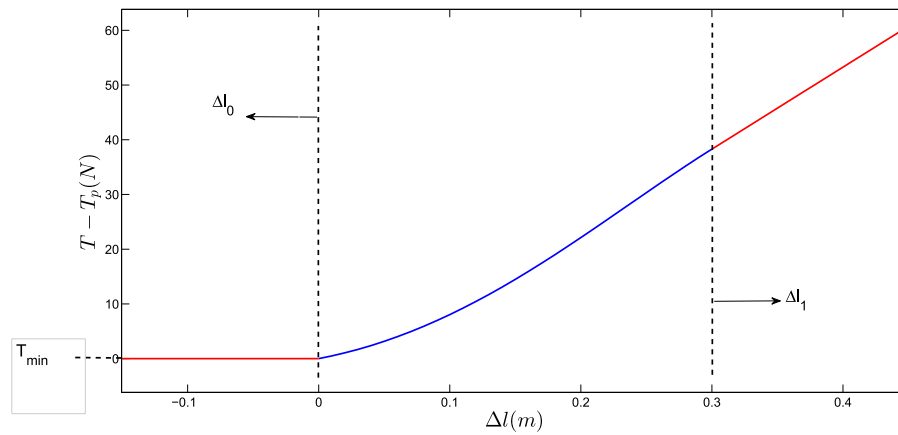
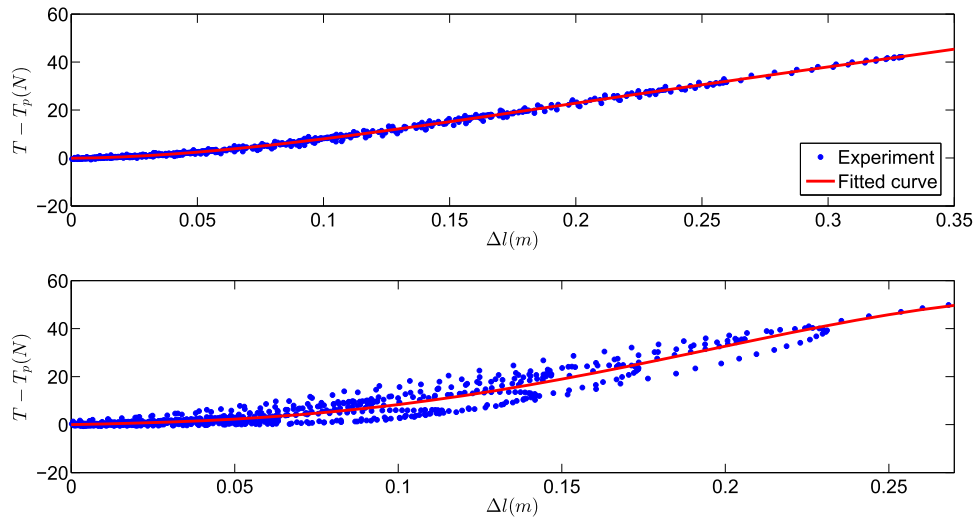**Fig. 9.** The tension versus cable length change.

Fig. 10. Cables tension versus length variation and related identification for surge decay test C451 for the fore (top) and aft (bottom) starboard cables.

Table 6
Mooring cables identification parameters for different cases.

	T_p (N)	T_{min} (N)	Δl_0 (m)	Δl_1 (m)	a_0 (N)	a_1 (N/m)	a_2 (N/m^2)	a_3 (N/m^3)	a_4 (N/m^4)
$Fn = 0$ bow cables	5.37	0	0	0.25	0	10.99	940.57	-2567.35	2404.84
$Fn = 0$ aft cables	10.44	0	0	0.15	0	52.91	-490.09	10833.44	-27828.92
$Fn = 0.09$ bow cables	30.8	-23.8	-0.2	0.2	0	151.08	14.35	-330.43	1976.84
$Fn = 0.09$ aft cables	32.86	-23.66	-0.12	0.13	0	300.50	-381.21	-4052.05	-3814.86
$Fn = 0.18$ bow cables C545	42.02	-23.8	-0.2	0.2	0	141.08	14.35	-230.43	1976.84
$Fn = 0.18$ aft cables C545	27.01	-23.66	-0.12	0.1	0	280.50	281.21	-3552.05	-3814.86
$Fn = 0.18$ bow cables other cases	42.02	-23.8	-0.2	0.2	0	141.08	14.35	-230.43	1976.84
$Fn = 0.18$ aft cables other cases	16.50	-23.66	0	0.1	0	50.98	551.68	2884.48	-9000.0

Table 7
Linear and quadratic damping coefficient as obtained from the free-decay analysis.

$B_{11}^{exp,lin}$ (Ns/m)	$B_{22}^{exp,lin}$ (Ns/m)	$B_{44}^{exp,lin}$ (Nms)	$B_{66}^{exp,lin}$ (Nms)
20.92 for $Fn=0$ test cases and 25.41 for other test cases	39.14	1.23	65.03
$B_{11}^{exp,quad}$ (Ns^2/m^2)	$B_{22}^{exp,quad}$ (Ns^2/m^2)	$B_{44}^{exp,quad}$ (Nms^2)	$B_{66}^{exp,quad}$ (Nms^2)
0	0	10.12	0

Fig. 16 examines case C483, which is associated with important PR caused by the steepest examined waves at frequency ratio of 0.48. The agreement between the two results is satisfactory (except for the transient part of the roll motion). It should be borne in mind that the important parameter in the PR analysis is its occurrence and steady-state roll amplitude. In a practical case, the build-up phase of the roll motion would also matter to characterize the time scale for PR to reach critical roll angles. However, in the experiments, this build-up phase is much affected by the used set up. In the experiments, the cables configuration and also lots of other asymmetric effects could trigger the PR while in the numerical simulations the cables are exactly symmetric and there are not the disturbances as in the experimental set-up.

For six cases (C473, C493, C464, C459, C480 and C482), highlighted in grey in Table 8, the numerical and experimental results are
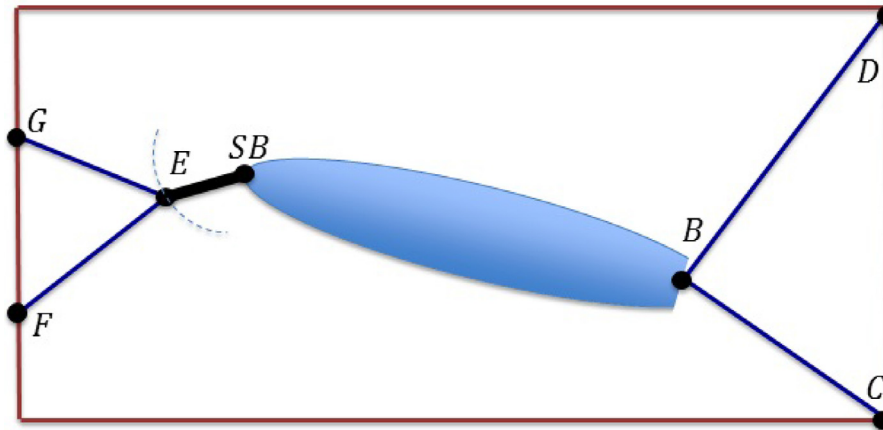
Fig. 11. Top view of the cable configuration with an arbitrary motion of the ship model.
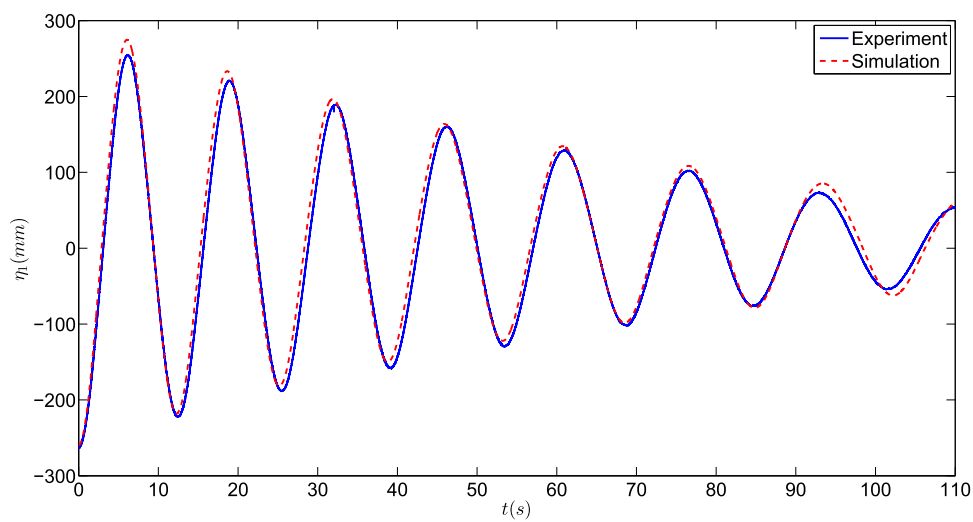

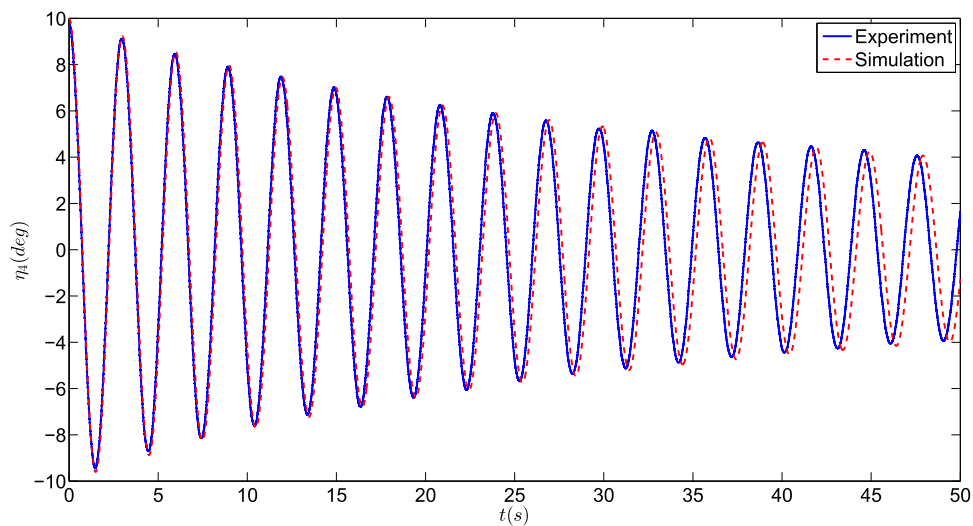**Fig. 12.** Comparison of numerical and experimental results for C451 surge decay test.

Fig. 13. Comparison of numerical and experimental results for C450 roll decay test.

somehow different. The numerical simulation shows PR in the cases near the instability border, while no PR was observed in experiments even with triggering a roll motion. This is examined in the following considering the ship-instability tendency in the experimental case and comparing this with the results from a Mathieu-type instability for the uncoupled roll equation of motion. The equation of uncoupled roll and the Mathieu-type instability diagram could be found in detail in [40].

If we calculate the metacentric-height variation for the SFH112 fishing vessel interacting with the waves in the Table 2, we can superimpose each experimental case as a point in the Mathieu-instability

Table 8

Test cases at $Fn = 0$, as given in Table 2. For each examined case, the experimental (Exp) and numerical (Num) roll-motion amplitudes in nearly steady-state conditions are given in degrees. A roll angle with a F shows that the roll steady-state value is obtained by forcing the model with a small roll angle if parametric-roll did not appear spontaneously. NOF means that parametric roll did not happen even with triggering the roll motion.

$k\zeta_a \downarrow \frac{\omega_{n4}}{\omega_e} \rightarrow$		0.46	0.47	0.48	0.49	0.50	0.51	0.52	0.53	0.54
0.10	Exp Num	X X	X X	C459 NOF 3.8	C479 21.1 19.2	C457 18.27 18.9	C501 15.24 16.75	C468 12.5 12.9	C480 NOF 11.0	X X
0.15	Exp Num	X X	C464 NOF 14.0	C463 23.66 21.8	C462 22.2 20.5	C461 20.76 18.9	C460 17.11 17.4	C469 16.0 14.5	C481 12.5 11.8	C482 NOF 7.7
0.20	Exp Num	C473 NOF 26.9	C472 19.2 25.0	C471 25.13 22.4	C470 22.52 20.7	C466 20.7 18.25	C465 17.0 16.0	C474 16.05 13.0	C484 10.5F 9.9	C499 5.0F 5.3
0.25	Exp Num	C493 NOF 25.7	C490 20.0 24.1	C483 24.6 21.0	C491 21.4 18.5	C492 18.1 16.0	C495 15.0 15.5	C496 13.7 12.0	C497 10.0F 11.0	C500 NOF NOF

diagram. The results are shown in Fig. 17. It should be noted that the effect of heave and pitch motions are also considered in the meta-centric-height calculations. The solid lines show the instability border for different damping values for the uncoupled roll equation of motion.

δGM is the metacentric-height variation (amplitude of oscillation) and GM_m is the metacentric height mean value. Symbol PR indicates cases in which parametric roll occurs. PR (F) means PR occurs but a forced roll should be introduced in the system, and No PR (F) means PR does not occur even by initiating, i.e. forcing, a roll motion. The parameter in the figure connected with the experimental damping ratio ξ, i.e. $\xi \frac{\omega_n}{\omega_e}$, for the examined cases is between 0.0014 and 0.0016. As it can be seen, it is obvious that the instability borders are a bit different from those in the Mathieu instability diagram. The instability region for the experiments covers a wider range of frequency ratio and the threshold value of metacentric height variation amplitude to have parametric roll seems to be lower than predicted by the 1-DOF Mathieu instability diagram. This is because the Mathieu-type equation is for an uncoupled roll equation and the GM variation is considered as a sinusoid while in reality the roll motion is coupled with other modes of motion and the GM variation in time is not exactly sinusoidal. As we can see from the figure, all the test cases with differences between numerical and experimental data, are at the instability borders. At the stability border, the roll behaviour is highly sensitive to the damping value and excitation level and other parameters. So, a small change in these parameters can lead us to go in the stability zone or get off that zone.

4.2. Cases at Fn = 0.09

The test matrix for the cases with Fn = 0.09 is shown in Table 3. The experimental and numerical results for roll-motion amplitude in nearly steady-state conditions in all studied cases are given in Table 9.

As it can be seen, the overall results are in good agreement in terms of PR occurrence and roll steady-state amplitude, but for three cases: C521, C537 and C535. These three cases are shown and discussed in more detail in the following.

For case C521 (see Fig. 18), by synchronizing roughly the numerical and experimental time evolutions, the numerical PR starts to grow when the experimental time history is over. At that time the amplitude of the numerical roll is less than 1°.

The same situation happens for case C537 (see Fig. 19) but the numerical roll amplitude at the end of the experimental time history is around 4°.

The scenario is different for case C535. In this case (see Fig. 20), the experimental pitch motion reduces strangely without reaching the steady state value. This reduction in pitch could avoid PR occurrence in the experiments. Checking the experimental video for this case did not help to find the reason of this pitch reduction. Although the heave motion is more regular then pitch motion, still it does not show a regular steady state oscillation which might be due to the not-regular incident wave.

For a better picture of the position of these three cases in the instability diagram, a numerical study was performed for several wave conditions with different wave frequency ratios $\frac{\omega_{n4}}{\omega_e}$ ranging from 0.40 to 0.51 and $k\zeta_a$ in the range from 0.05 to 0.20. The results are presented in Fig. 21. Also in this case PR and No PR mean, respectively, parametric-resonance occurrence or else.

From the figure, the cases C537 and C521 are clearly at the stability border. But case C535 seems to be well inside the instability region. The latter is because for all cases with higher frequency ratio ($\frac{\omega_{n4}}{\omega_e} = 0.51$) and all wave steepnesses, PR was observed. This supports the idea that something happened in the experiments in this case, reducing the pitch amplitude with respect to the initial steady-state tendency and therefore preventing PR occurrence.
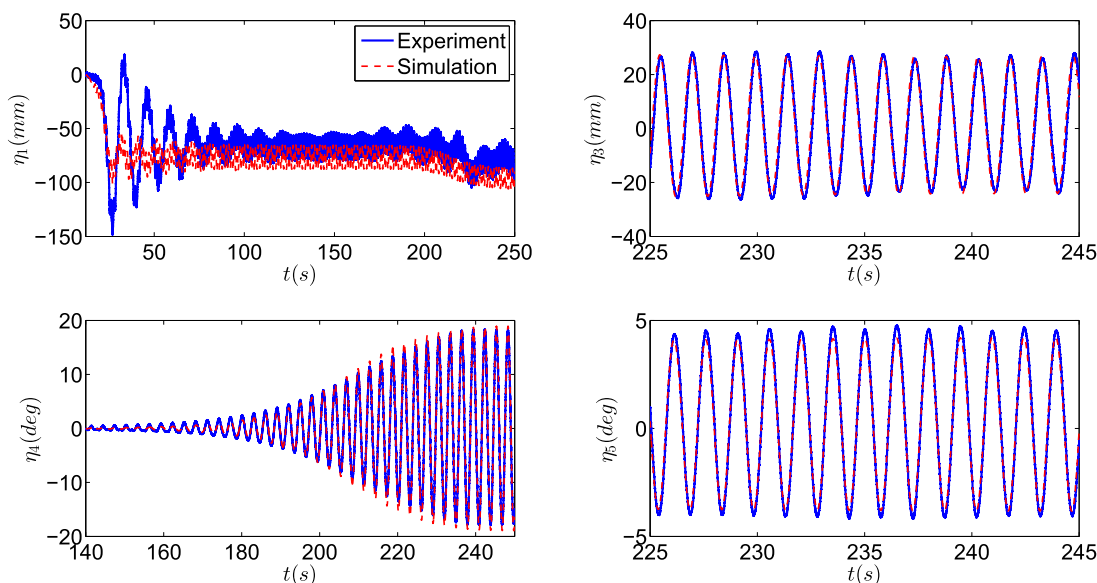
Fig. 14. Comparison of experimental and numerical motions in selected degrees of freedom for case C457.
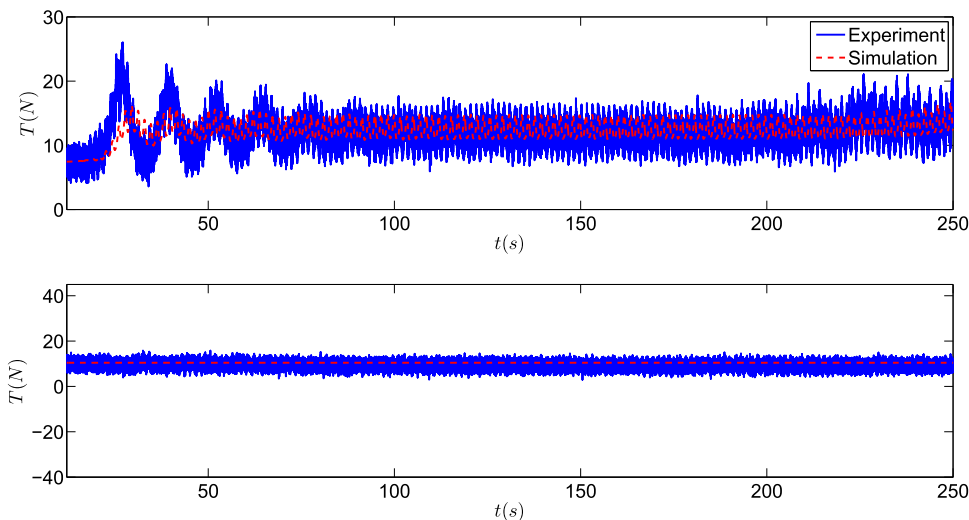

Fig. 15. Comparison of experimental and numerical values for mooring cables tensions in case C457. Fore cable tension (top) and aft cable tension(bottom).

4.3. Cases at Fn = 0.18

The test matrix for the cases with Fn = 0.18 is shown in Table 4. The experimental and numerical comparison in PR occurrence and severity for all examined cases is shown in Table 10. For consistency, the ship trim and sinkage observed in the experiments at this forward speed were included in the simulations.

From the table, the numerical and experimental results disagree in terms of PR occurrence for two cases, i.e. C555 and C545. In the other cases, the numerics predicts well the PR occurrence but the roll amplitude tends to over-predict the experimental value. A detailed analysis of the individual cases is presented next. From now on, we refer to the nominal wave characteristics of the cases for sake of simplicity.

Fig. 22 presents the comparison of the experimental and numerical roll motion for case C555. This corresponds to the lowest examined wave-frequency ratio. Experimentally no PR is observed, even with triggering the roll motion. Numerically, a PR with amplitude 27.5° develops at a time later than when the roll motion is triggered without PR in the experiments. Considering the nominal-wave parameters, in this case the wave-frequency ratio is $\frac{\omega_{n4}}{\omega_e} = 0.43$ and the wave steepness is $k\zeta_a = 0.15$. At the same wave steepness and increasing the nominal

wave frequency ratio to $\frac{\omega_{n4}}{\omega_e} = 0.44$ and 0.45, the PR is observed experimentally after forcing a roll motion. Therefore we can say that the left instability border for the nominal wave steepness $k\zeta_a = 0.15$, is at a frequency ratio between 0.43 and 0.44. This suggests that the difference in PR occurrence for case C555 might be due to the case being close to the instability border and therefore to a greater sensitivity of the vessel behaviour to the involved roll damping.

Figs. 23 presents the comparison of the experimental and numerical roll motion for case 554 with nominal frequency ratio $\frac{\omega_{n4}}{\omega_e} = 0.44$ and nominal wave steepness $k\zeta_a = 0.15$. In this case, a PR with value of 14.5° is observed experimentally with a forced roll motion. In the numerical simulations, a PR with value 27.0° occurs, without the need of forcing the roll motion. The reason for the large difference in steady-state roll amplitude lies in the complicated non-linearities involved for this wave-body interaction case, which are not fully handled in the proposed numerical model. At this forward speed and wave parameters, huge amount of wave breaking in the ship bow and huge bottom slamming and bow flare slamming and even water on deck are observed experimentally. Bottom slamming and water shipping are modeled in our solution strategy but in the simulations they appear quite mild. A possible explanation is that, in the experiments they are triggered by
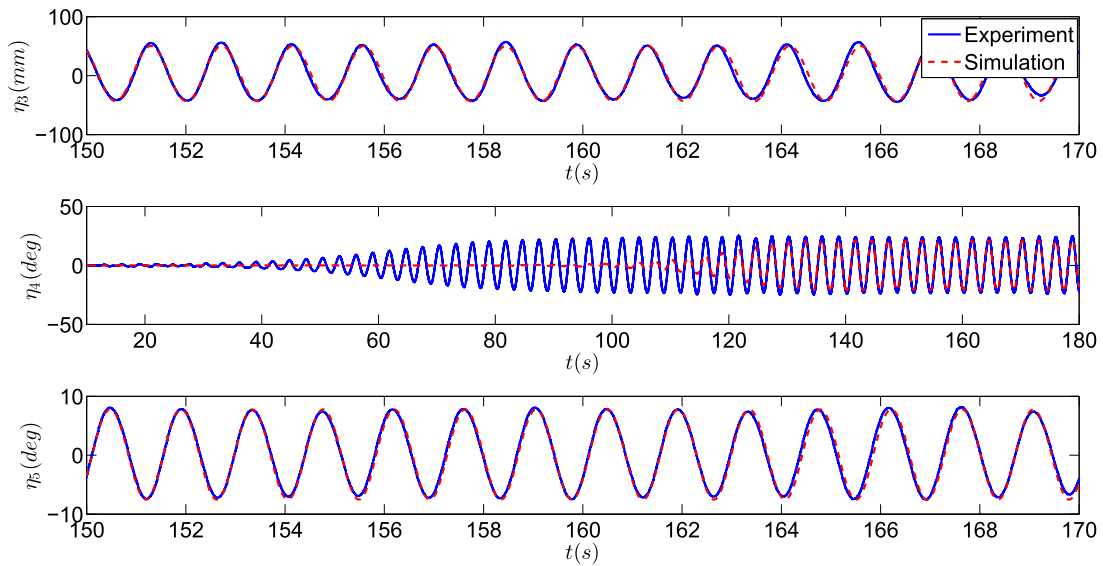
13

Fig. 16. Comparison of experimental and numerical incident waves and model motions in all six degrees of freedom for case C483.
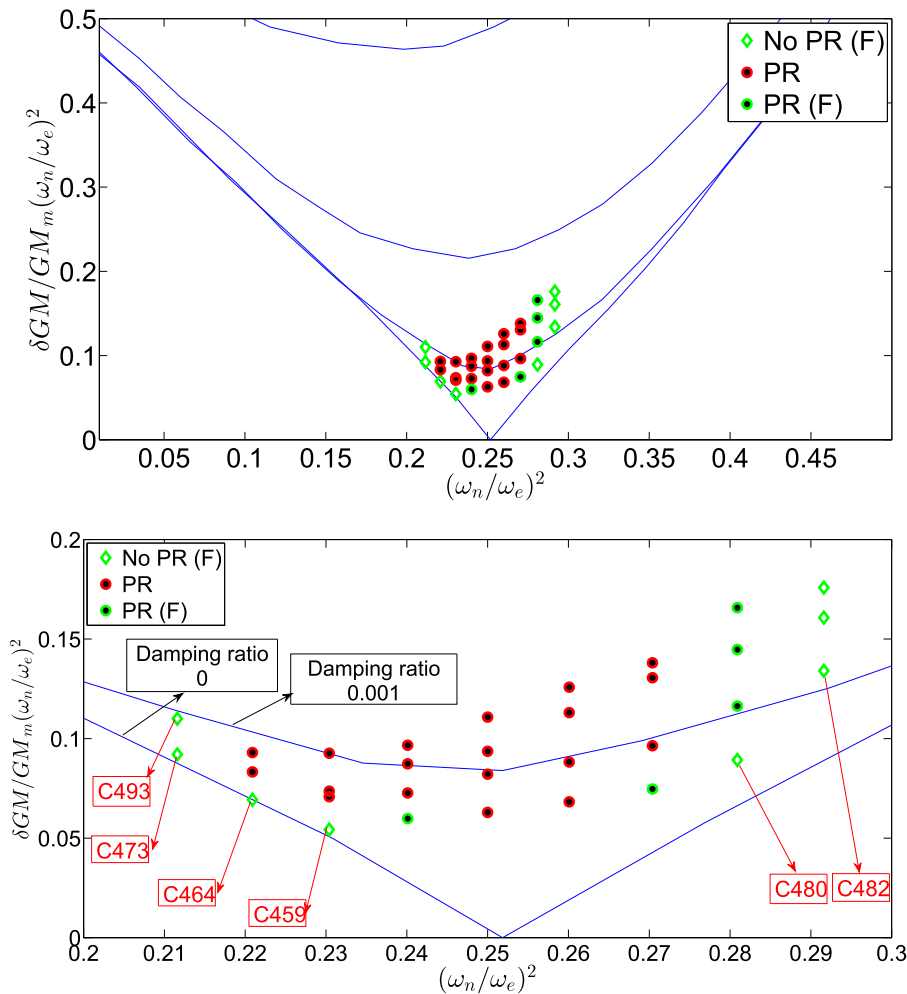

Fig. 17. Mathieu instability diagram for uncoupled roll (solid lines) and experimental cases (symbols) at Fn = 0. Main plot (top) and enlarged view (bottom).

stronger nonlinear phenomena than those accounted for by the numerics. Fig. 24 shows snapshots of water on deck phenomenon and bottom and bow flare slamming in this experimental case.

Figs. 25 and 26, present the comparison of the roll motions, respectively for cases C551 and C550. They correspond to nominal wave-

frequency ratio $\frac{\omega_{n4}}{\omega_e} = 0.45$ and 0.46 and the wave steepness $k\zeta_a = 0.15$. For them, we observe the PR occurrence in the experiments after a forced roll motion. The numerical results show the PR occurrence without forcing a roll motion, with larger value than experimentally. In both cases PR developed at a time later than when the roll motion is

Table 9

Test cases at Fn = 0.09, as given in Table 3. For each examined case, the experimental (Exp) and numerical (Num) roll-motion amplitudes in nearly steady-state conditions are given in degrees. A roll angle with a F shows that the roll steady-state value is obtained by forcing the model with a roll angle if parametric-roll did not appear spontaneously. NOF means that parametric roll did not happen even with triggering the roll motion.

$k\zeta_a\downarrow, \frac{\omega_{n4}}{\omega_e}\rightarrow$	0.45	0.46	0.47	0.48	0.49	0.50
0.10 Exp Num	X X	X X	C521 NO 30.0	C538 23.5F 25.6	X X	X X
0.15 Exp Num	C537 NOF 30.0	C536 24.0F 24.5	C522 16.5F 23.0	C533 22.5F 22.4	C534 18.5F 20.5	C535 NOF 19.3
0.20 Exp Num	X X	X X	X X	C539 15.3F 19.0	X X	X X
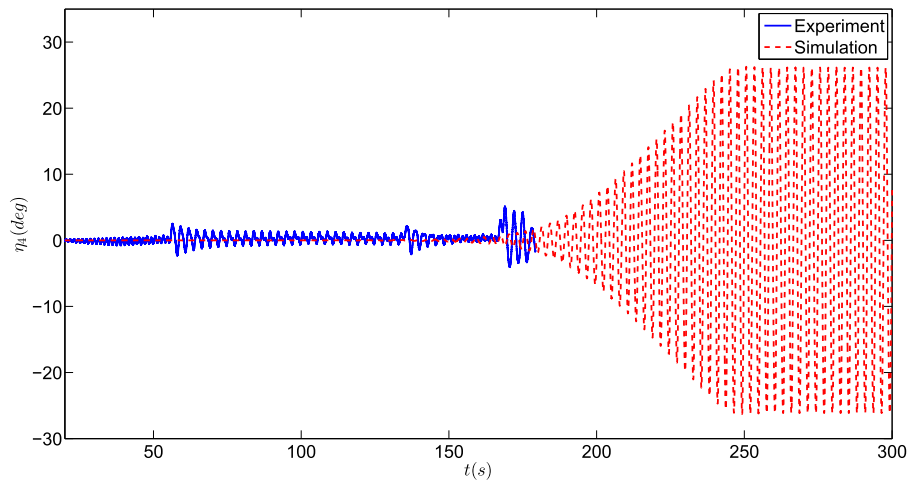
Fig. 18. Comparison of experimental and numerical roll motion for case C521.
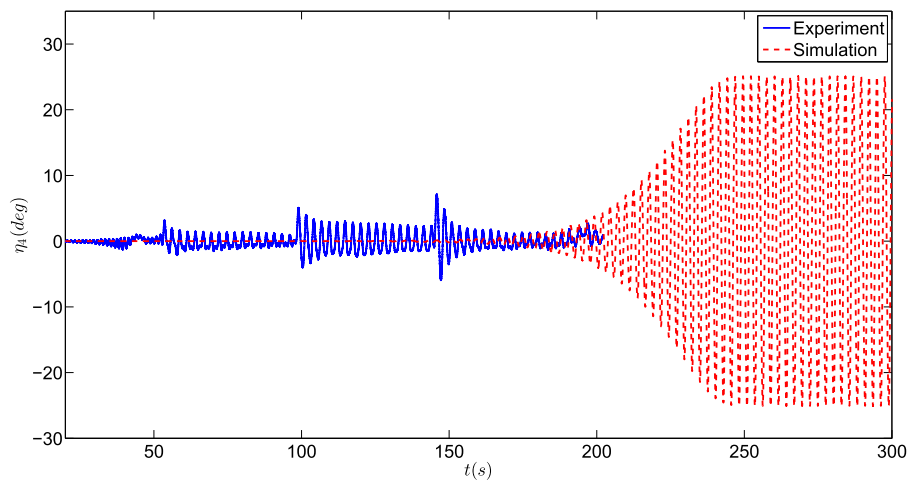
Fig. 19. Comparison of experimental and numerical roll motion for case C537.

triggered in the corresponding experiments. Forcing the roll motion in the numerical simulations gives the same amplitude for the PR as obtained without any triggering mechanism (not shown here).

Fig. 27 presents the comparison of the roll motion for case 549, with nominal wave-frequency ratio $\frac{\omega_{n4}}{\omega_e} = 0.47$ and the same wave steepness as for the cases with Fn = 0.18 examined so far. In this case, a PR with amplitude of 18° is observed in the experiments with a triggered roll motion. Numerically, the simulation performed without forcing the roll motion predicts no PR occurrence. Then we tried to trigger a roll motion in this case similarly as in the experiments. This was done enforcing a Gaussian roll moment for a very short time. By doing so, a PR with amplitude of almost 23° builds up. This value is relatively close to the experimental results, as shown in Fig. 27.

Fig. 28 presents the comparison of the roll motion for case C548, with nominal wave-frequency ratio $\frac{\omega_{n4}}{\omega_e} = 0.48$ and wave steepness

$k\zeta_a = 0.10$. In this case, a PR with amplitude of 21° is observed experimentally after triggering a roll motion. The numerical simulations also show a PR with amplitude of 25°. Fig. 29 presents the comparison of the motions for case C545, with larger nominal wave steepness, i.e. $k\zeta_a = 0.15$, and the same nominal wave frequency ratio as for C548. For this case, experimentally no parametric resonance is observed even after triggering the parametric roll. Numerically the PR occurs on a long time scale. Slightly after the numerical PR starts to develop, experimentally something happened as indicated by a sign change in surge (at a time of about 75 s), that goes from a saturated negative value to a large positive value. Shortly after, large sway oscillations are triggered, coupled with yaw. It is hard from the vessel motions to identify the physical phenomenon occurred in the model tests, but its excitation of sway and yaw motions could be responsible for preventing the PR occurrence in the experiments. As a result, we cannot conclude about the PR occurrence in the experiments for this case. The cables tensions for
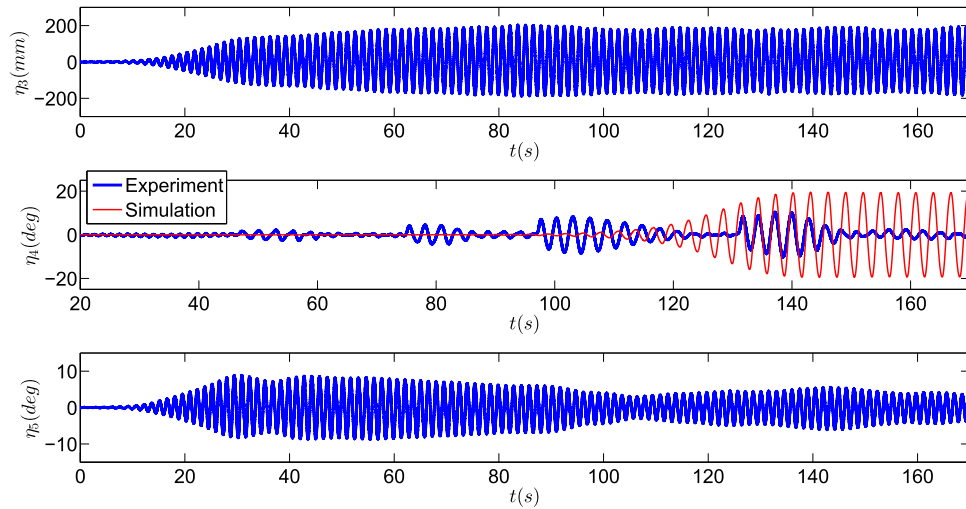
Fig. 20. Top: Comparison of experimental and numerical roll motion for case C535 (middle). Top and bottom: Experimental heave and pitch motions for case C535.
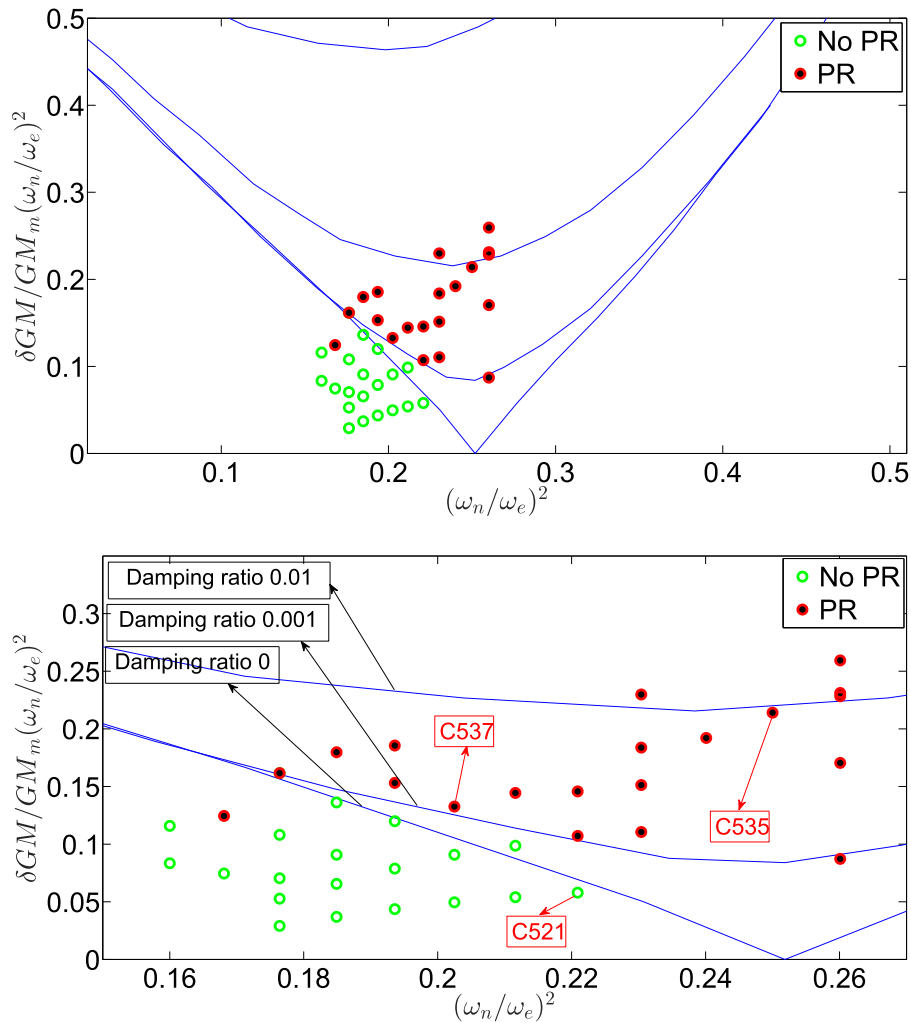

Fig. 21. Mathieu instability diagram for uncoupled roll (solid lines) and numerical cases (symbols) at Fn = 0.09. Main plot (top), enlarged view (bottom).

this case are also shown in Fig. 30. As it can be seen in this figure, while the fore cables tensions are in good agreement, the aft cables do not show that level of agreement which might be due to the differences in the surge excursion. Some differences can also be seen in the beginning of the simulation in both fore and aft cables, which are due to the differences in surge motion in the transient phase.

Fig. 31 presents the comparison of the roll motion for case C552, with nominal wave frequency ratio $\frac{\omega_{n4}}{\omega_e} = 0.49$ and the nominal wave steepness $k\zeta_a = 0.15$. In this case, experimentally a triggered roll motion leads to a PR with amplitude around 9°. The numerical simulation, without a roll-forcing mechanism, indicates no parametric roll. Triggering a roll motion as in the experiments leads to PR occurrence with

Table 10

Test cases at Fn = 0.18, as given in Tab 4. For each examined case, the experimental (Exp) and numerical (Num) roll-motion amplitudes in nearly steady-state conditions are given in degrees. A roll angle with a F shows that the roll steady-state value is obtained by forcing the model with a roll angle if parametric-roll did not appear spontaneously. NOF means that parametric roll did not happen even with triggering the roll motion.

$k\zeta_a\downarrow,\frac{\omega_{n4}}{\omega_e}\rightarrow$	0.43	0.44	0.45	0.46	0.47	0.48	0.49	0.50
0.10 Exp Num	X	X	X	X	X	C548 21.1F 25.0	X	X
0.15 Exp Num	C555 NOF 27.5	C554 14.5F 27.0	C551 18.5F 26.5	C550 20.6F 25.6	C549 18F 23.0F	C545 NOF 20.2	C552 9F 15.0F	C553 NOF NOF
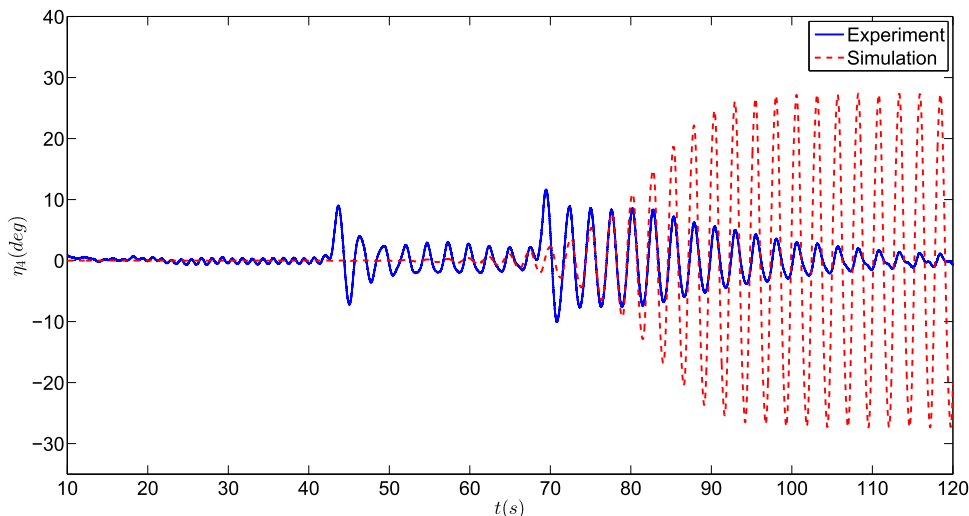
Fig. 22. Comparison of experimental and numerical roll motion for case C555.
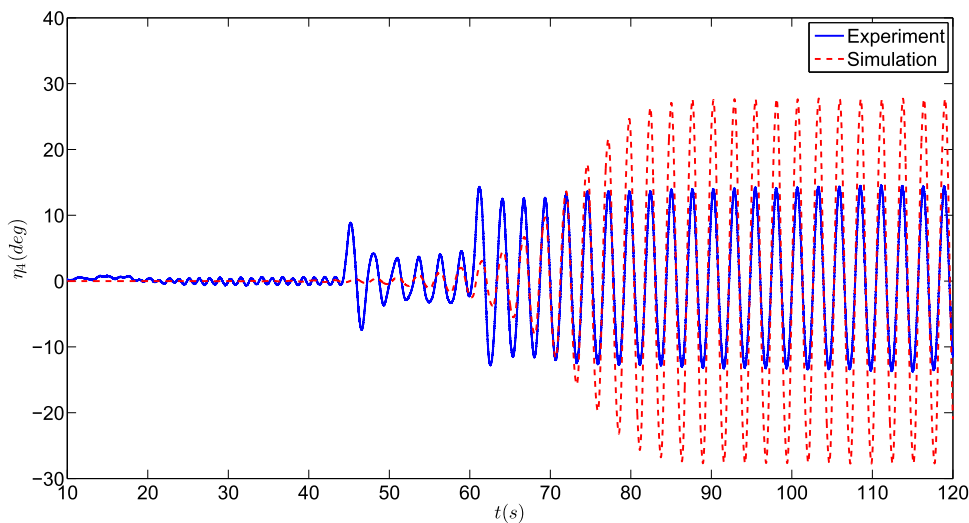
Fig. 23. Comparison of experimental and numerical roll motion for case C554.

amplitude 15°, as shown in Fig. 31.

Fig. 32 presents the comparison of the roll motion for case C553, representing the last examined case in this section. It is associated with nominal wave-frequency ratio $\frac{\omega_{n4}}{\omega_e} = 0.50$ and wave steepness $k\zeta_a = 0.15$. The experimental results show no PR even with forcing a roll motion. The forced roll motion is damped out after some oscillations. The numerical results without forcing a roll motion showed no parametric resonance. They were then repeated enforcing a roll motion similarly as forced in the experiments. The new results confirmed no PR for this case. Since case C553 is associated with no PR and case C552 has a PR with small amplitude, it seems that the instability border is somewhere between frequency ratio $\frac{\omega_{n4}}{\omega_e} = 0.49$ and 0.50.

5. Effect of weak-scatterer assumption

The effect of using weak-scatterer assumption in the numerical simulation is assessed with running the numerical simulations with and without it for cases at $Fn = 0$. The comparison of the results is documented in Table 11.

The results with a difference in roll amplitude larger than 5° between the numerical solutions with and without weak-scatterer assumption are highlighted in grey in the table. As it can be seen and consistently with the inherent features, the weak scatterer assumption is highly important for higher frequency ratios (longer waves) and steeper waves. The solver without weak-scatterer assumption can capture all experimental results only for frequency ratio 0.48, correctly. For
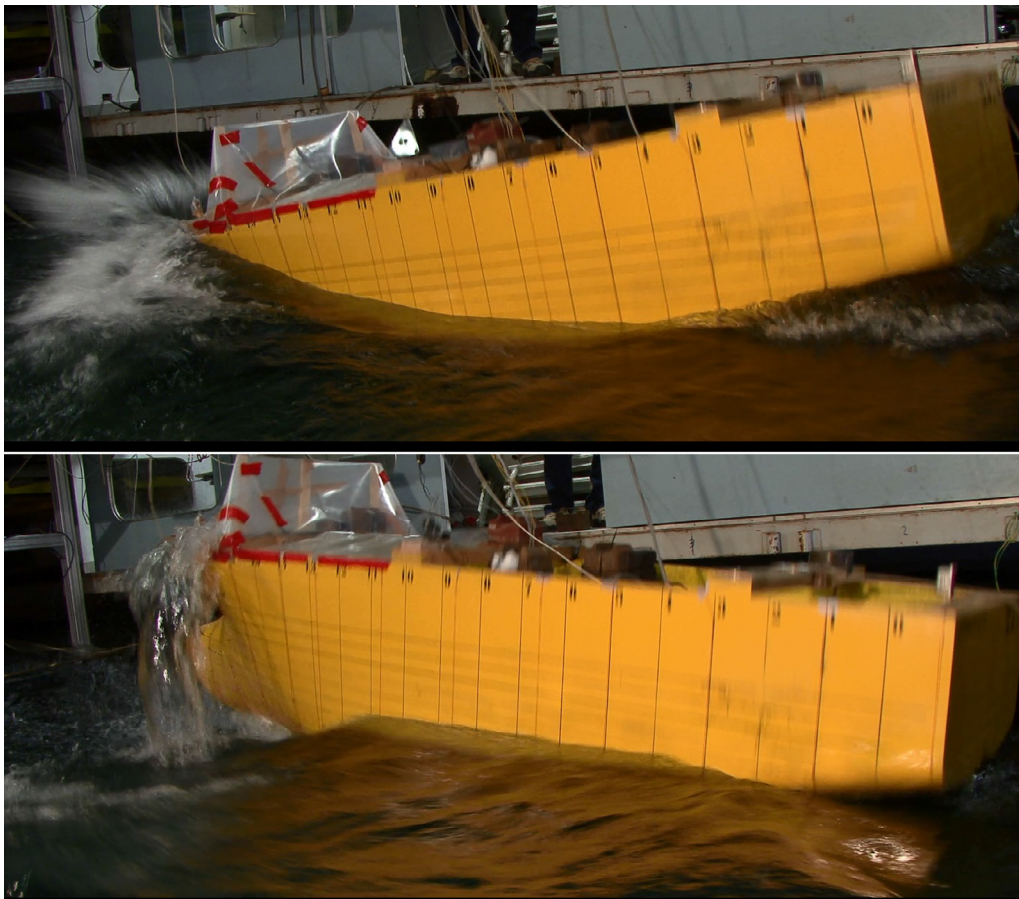
Fig. 24. Snapshots of experiment case C554. Top: Bottom and bow flare slamming. Bottom: Water on deck phenomenon.
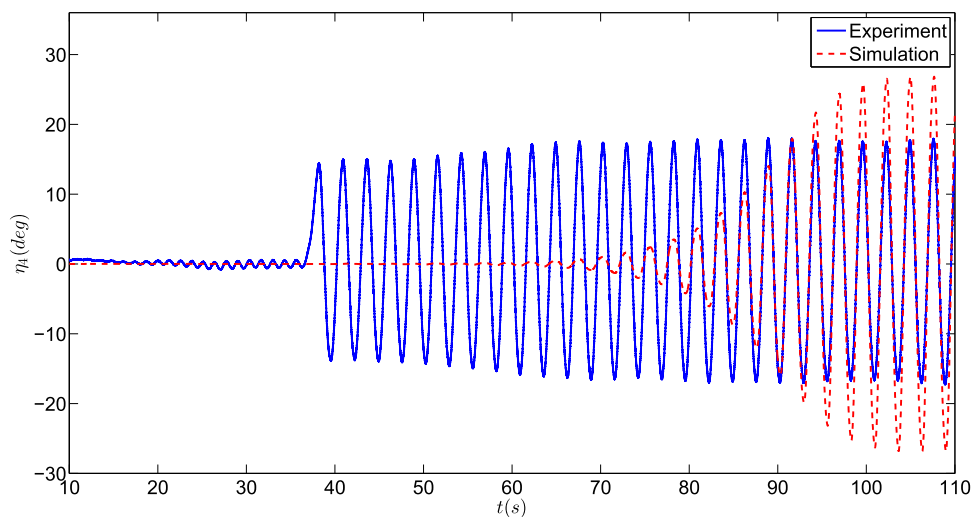

Fig. 25. Comparison of experimental and numerical roll motion for case C551.

the examined cases and for this vessel, the results using weak-scatterer assumption are more consistent with the experiments than the results without weak-scatterer. The results show that the simulations without this hypothesis tend to underestimate the occurrence and severity of parametric roll. This underestimation increases in longer and steeper waves.

6. Summary and conclusion

A combined numerical-experimental study on the parametric roll of the fishing vessel SFH112 without forward speed ($Fn = 0$) and with two different forward speeds ($Fn = 0.09$ and $Fn = 0.18$) and in head-sea regular waves has been presented. Numerically, it is used a blended method with linear radiation and diffraction corrected within the weak-scatterer assumption. In the physical tests, a cable system was used to limit mean horizontal motion of the vessel and was consistently modeled in the simulations. The cables have the most effects in the surge motion and the surge excursion is important in the roll motion. We tested this numerically. The results showed that the surge motion has effects in both parametric roll occurrence in some cases and steady state
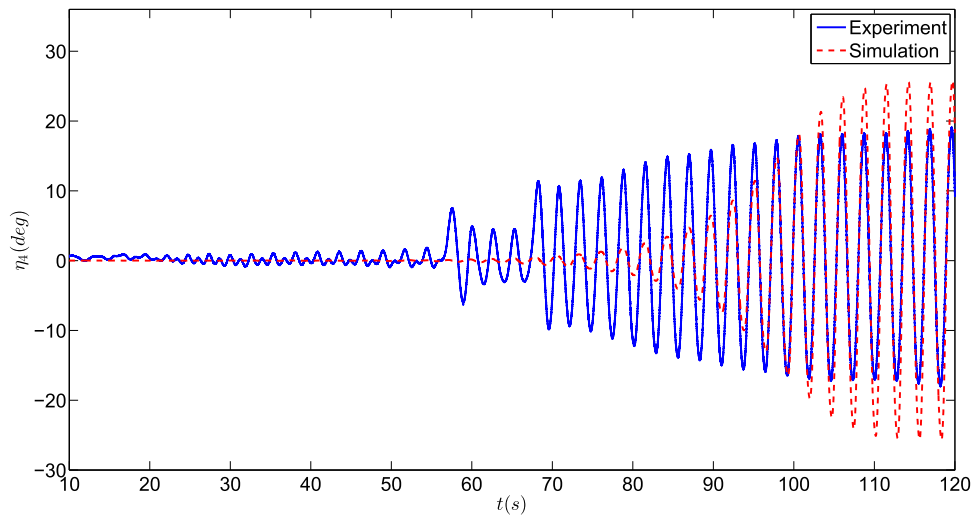
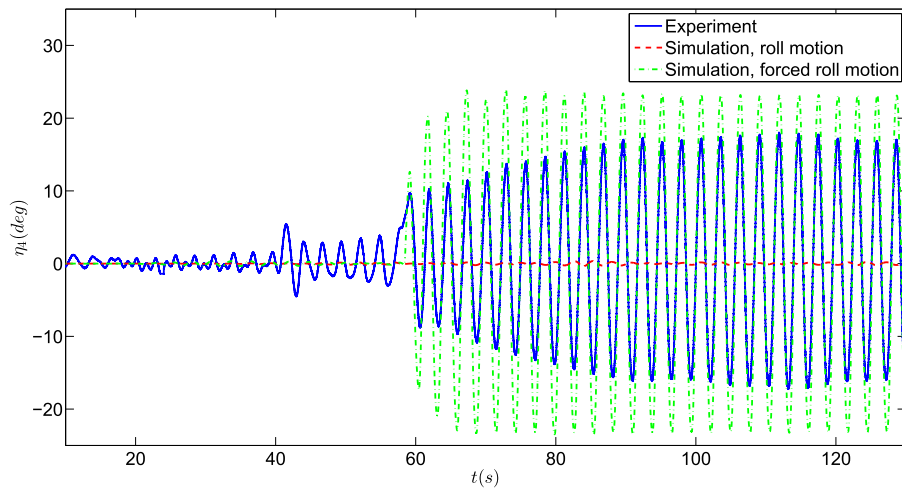**Fig. 26.** Comparison of experimental and numerical roll motion for case C550.

Fig. 27. Comparison of experimental and numerical roll motion for case C549.
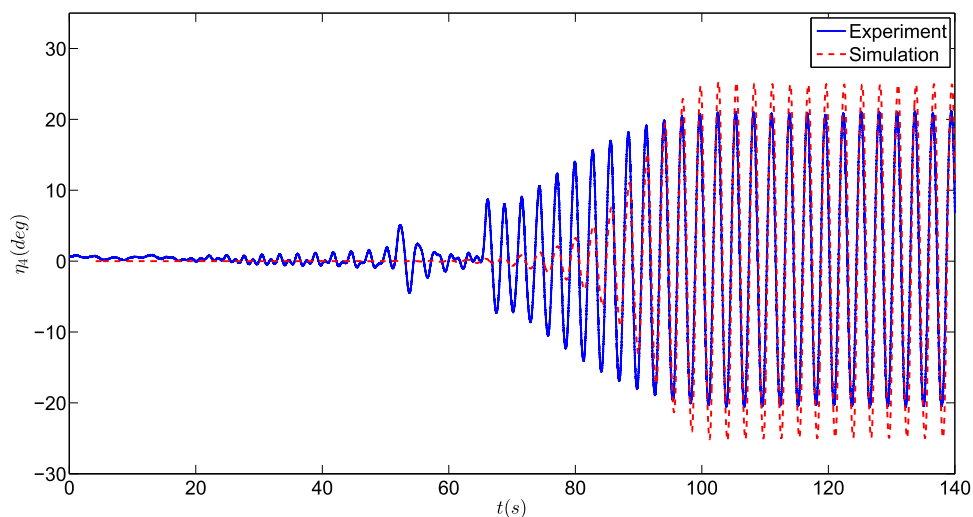

Fig. 28. Comparison of experimental and numerical roll motion for case C548.

roll amplitude in some other cases. The results for this study are presented in Table 8.2 in [32]. The experiments were performed with different wave periods and steepnesses. Free-decay tests were performed to identify the damping in the tests and the cable tensions. The viscous roll damping, the linear incident-wave parameters and the cable tensions, identified from the tests, were used as input in the simulations.

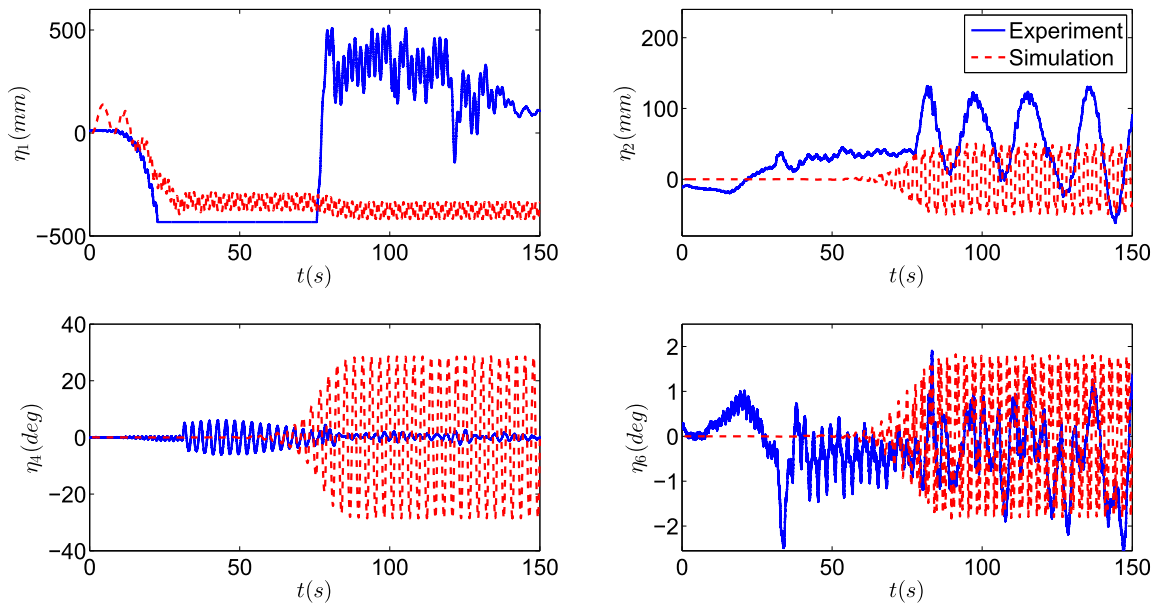In general experimental and numerical results at all Fn values

Fig. 29. Comparison of experimental and numerical motions in selected degrees of freedom for case C545.
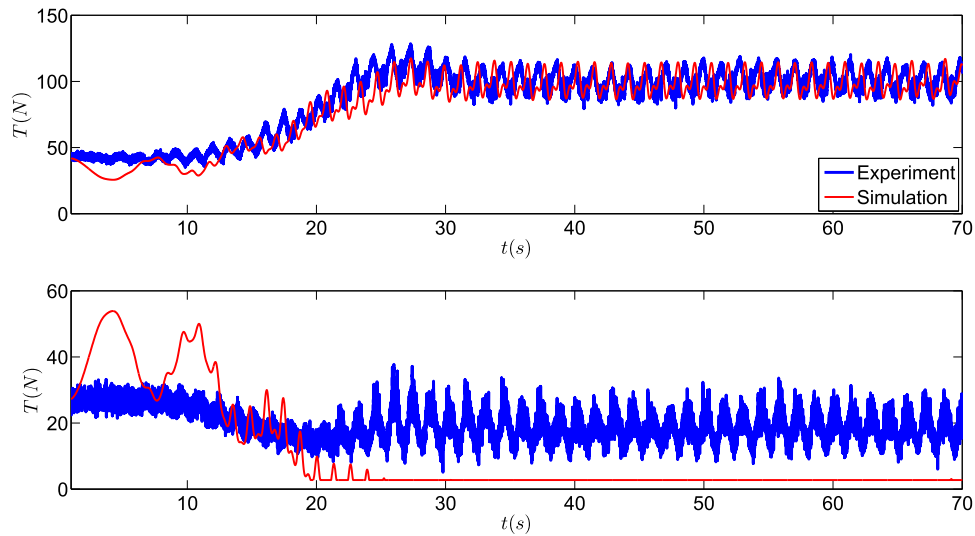

Fig. 30. Comparison of experimental and numerical values for mooring cables tensions in case C545. Fore cable tension (top) and aft cable tension(bottom).
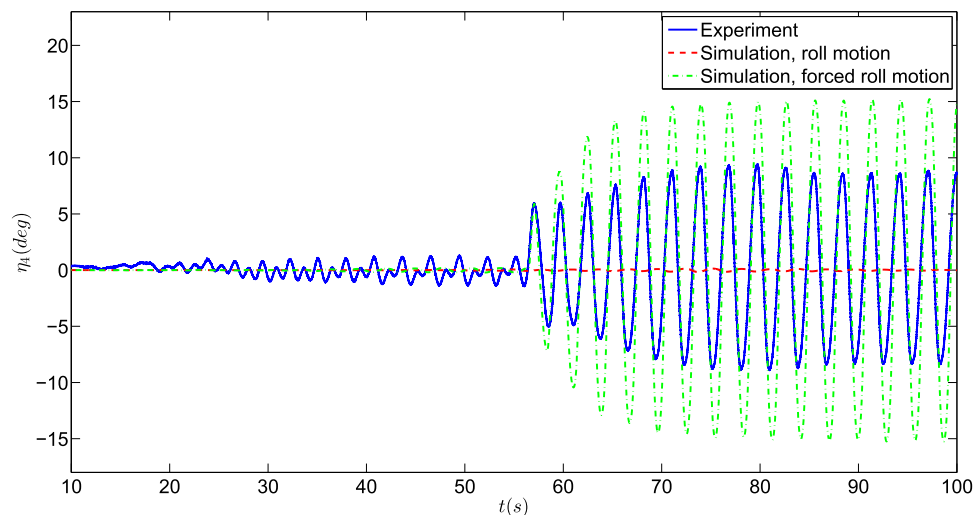

Fig. 31. Comparison of experimental and numerical roll motion for case C552.
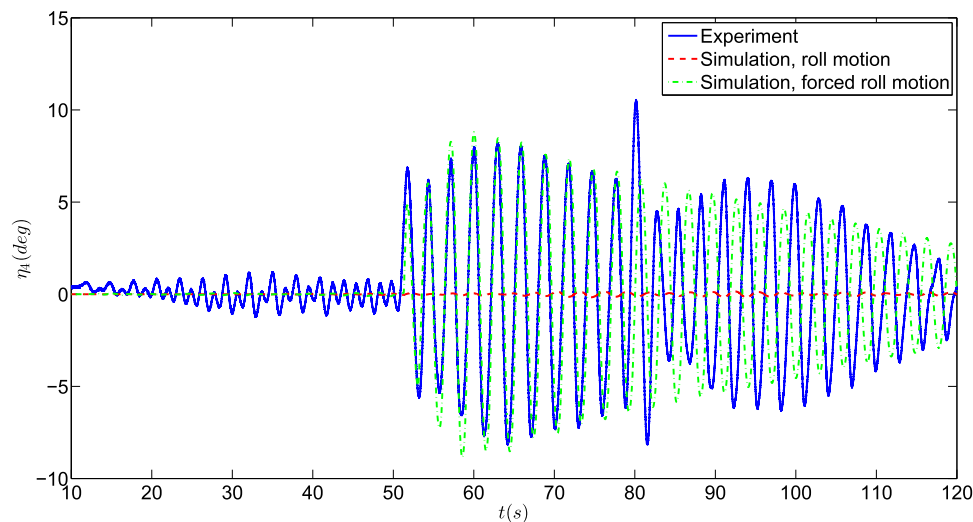
Fig. 32. Comparison of experimental and numerical roll motion for case C553.

Table 11
Test cases at $Fn = 0$, as given in Table 2. For each examined case, the experimental (Exp), numerical with weak-scatterer assumption (Num WS) and numerical without weak-scatterer assumption (Num NoWS) roll-motion amplitudes in nearly steady-state conditions are given in degrees. A roll angle with a F shows that the roll steady-state value is obtained by forcing the model with a small roll angle. NOF means that parametric roll did not occur even with triggering the roll motion.

$k\zeta_a \downarrow, \frac{\omega_{n4}}{\omega_e} \rightarrow$	0.48	0.49	0.50	0.51
0.10 Exp Num WS Num NoWS	C459 NOF 3.8 3.7	C479 21.1 19.2 18.0	C457 18.27 18.9 16.5	C501 15.24 16.75 10.5
0.15 Exp Num WS Num NoWS	C463 23.66 21.8 18.5	C462 22.2 20.5 16.5	C461 20.76 18.9 5.0	C460 17.11 17.4 NOF
0.20 Exp Num WS Num NoWS	C471 25.13 22.4 19.0	C470 22.52 20.7 12.2	C466 20.7 18.25 NOF	C465 17.0 16.0 NOF
0.25 Exp Num WS Num NoWS	C483 24.6 21.0 20.0	C491 21.4 18.5 NOF	C492 18.1 16.0 NOF	C495 15.0 15.5 NOF

examined agree in terms of PR occurrence and are consistent in most of the cases in terms of steady-state roll amplitude. In few cases the PR occurrence was not consistent, this was mainly for cases near the stability border and therefore more sensitive to the involved damping level, or due to some peculiar phenomena occurring in the experiments.

In some cases, triggering an initial roll angle makes the PR to occur while PR was not observed spontaneously without triggering (for example case C549). Such coexisting steady states might be explained as a result of sub-critical bifurcation, but it needs more investigation. Some recent papers have investigated this phenomenon in parametric rolling from the viewpoint of nonlinear dynamics or bifurcation theory [41,42].

There are numerical and experimental error sources that might have influenced the results. In the experiments, the heave and pitch motions are not very regularly oscillating even in the steady-state phase for all cases. That is partly due to the incident waves which are not perfectly regular because of reflection of waves from the tank walls. There are many non-linearities connected to the breaking waves at the ship bow observed for many cases (especially for cases with forward speed), to the bottom and bow flare slamming and even to water on deck in some cases. Small misalignments from the head sea waves in the experiments might also have some influences. The asymmetric cables in port and starboard are also important. Besides, in the numerical side, the interaction between the local steady flow and unsteady flow, for the advancing vessel, is ignored in the numerical solver. It might have some effects on the results especially for this ship, which is not slender. Furthermore, the non-linearities that are included in the numerical solver are simplified. Also local wave elevation (radiation and diffraction waves) is not considered in the wetted surface of the body in time.

The experimental results for Fn=0 and Fn=0.09 show that the stability border for the model in experiments is different from the 1-DOF Mathieu-type instability diagram. The instability region for the experiments covers a wider range of frequency ratio and the threshold

value of metacentric height variation amplitude for parametric roll seems to be lower than in the 1-DOF Mathieu-type instability diagram. The reasons are related to the non-linear variation of restoring and nonlinear damping mechanisms involved in the physical system. Besides, for these experiments the ship behaves strongly as a 6-DOF system in the context of PR occurrence and the roll was coupled to other modes of motions. The results also show that the instability region for the cases with forward speed shifts to the lower frequency ratios (natural roll frequency to encounter frequency ratio) compared to the cases without forward speed.

The effect of using the weak-scatterer assumption in modifying the radiation and diffraction loads is also modelled and studied in this study. It was shown that the weak-scatterer hypothesis can provide a more accurate prediction of the parametric roll. The results show that the simulations without this hypothesis tend to underestimate the occurrence and severity of parametric roll. This underestimation increases in longer and steeper waves.

Declaration of Competing Interest

The authors declare that they have no known competing financial interests or personal relationships that could have appeared to influence the work reported in this paper.

Acknowledgements

References

[1] W.N. France, M. Levadou, T.W. Treakle, J.R. Paulling, R.K. Michel, C. Moore, An investigation of head-sea parametric rolling and its influence on container lashing systems, Mar. Technol. 40 (1) (2003) 1–19.

[2] C. Holden, Modeling and control of parametric roll resonance(2011).

[3] Cargolaw.com, 2017.

[4] A.B. Dunwoody, Roll of a ship in astern seas–metacentric height spectra, J. Ship Res. 33 (3) (1989).

[5] A. Dunwoody, Roll of a ship in astern seas–response to gm fluctuations, J. Ship Res. 33 (4) (1989).

[6] N. Umeda, M. Hamamoto, Y. Takaishi, Y. Chiba, A. Matsuda, W. Sera, S. Suzuki, K. Spyrou, K. Watanabe, Model experiments of ship capsize in astern seas, J. Soc. Naval Archit. Jpn. 1995 (177) (1995) 207–217.

[7] N. Sanchez, A. Nayfeh, Nonlinear rolling motions of ships in longitudinal waves, Int. Shipbuild. Prog. 37 (411) (1990).

[8] I. Oh, A. Nayfeh, D. Mook, A theoretical and experimental investigation of indirectly excited roll motion in ships, Philos. Trans. R. Soc. Lond. A 358 (1771) (2000) 1853–1881.

[9] M. Hamamoto, J.P. Panjaitan, A critical situation leading to capsize of ships in astern seas, J. Soc. Naval Archit. Jpn. 1996 (180) (1996) 215–221.

[10] A. Munif, N. Umeda, Modeling extreme roll motions and capsizing of a moderate-speed ship in astern waves, J. Soc. Naval Archit. Jpn. 2000 (187) (2000) 51–58.

[11] N. PEREZ M, C. SANGUINETTI V, Experimental results of parametric resonance phenomenon of roll motion in longitudinal waves for small fishing vessels, Int. Shipbuild. Prog. 42 (431) (1995) 221–234.

[12] M. Neves, N. Pérez, L. Valerio, Stability of small fishing vessels in longitudinal waves, Ocean Eng. 26 (12) (1999) 1389–1419.

[13] M.A. Neves, On the excitation of combination modes associated with parametric resonance in waves, Proceedings of the 6th International Ship Stability Workshop, (2002).

[14] M.A. Neves, C.A. Rodríguez, An investigation on roll parametric resonance in regular waves, Int. Shipbuild. Prog. 54 (4) (2007) 207–225.

[15] A. Francescutto, An experimental investigation of parametric rolling in head waves, Trans.-Am. Soc. Mech. Eng. J. Offsh. Mech. Arct. Eng. 123 (2) (2001) 65–69.

[16] A. Francescutto, G. Bulian, C. Lugni, Nonlinear and stochastic aspects of parametric rolling modeling, Mar. Technol. 41 (2) (2004) 74–81.

[17] M. Palmquist, C. Nygren, Recordings of head-sea parametric rolling on a pctc, Annex in IMO SLF, 47 (2004).

[18] K. Spyrou, Design criteria for parametric rolling, Ocean. Eng. Int. 9 (1) (2005) 11.

[19] I. 2006, Recomended procedures and guidelines–testing and extrapolation methods loads and responses, stability predicting the occurrence and magnitude of parametric rolling, 2006.

[20] M. Levadou, G. Gaillarde, Operational guidance to avoid parametric roll, Proc. Int. Conf. on Design and Operation of Container Ships, (2003), pp. 75–86.

[21] Y. Shin, V. Belenky, J. Paulling, K. Weems, W. Lin, K. Mctaggart, K.J. Spyrou, T.W. Treakle, M. Levadou, B.L. Hutchison, et al., Criteria for parametric roll of large containerships in longitudinal seas, Trans.-Soc. Naval Archit. Mar.Eng. 112 (2004) 14–47.

[22] S. Silva, T. Santos, C.G. Soares, Parametrically excited roll in regular and irregular head seas, Int. Shipbuild. Prog. 52 (1) (2005) 29–56.

[23] M. Levadou, R. Vant Veer, Parametric roll and ship design(2011) 307–330.

[24] L.S. McCue, B.L. Campbell, W.F. Belknap, On the parametric resonance of tumblehome hullforms in a longitudinal seaway, Nav. Eng. J. 119 (3) (2007) 35–44.

[25] K. Spyrou, I. Tigkas, G. Scanferla, N. Pallikaropoulos, N. Themelis, Prediction potential of the parametric rolling behaviour of a post-panamax containership, Ocean Eng. 35 (11) (2008) 1235–1244.

[26] V.L. Belenky, K.M. Weems, W.-M. Lin, J.R. Paulling, Probabilistic analysis of roll parametric resonance in head seas, Contemporary Ideas on Ship Stability and Capsizing in Waves, Springer, 2011, pp. 555–569.

[27] G. Bulian, C. Lugni, A. Francescutto, A contribution on the problem of practical ergodicity of parametric roll in longitudinal long crested irregular sea, 7th International Ship Stability Workshop, (2004), pp. 101–117.

[28] G. Bulian, A. Francescutto, C. Lugni, On the nonlinear modeling of parametric rolling in regular and irregular waves, Int. Shipbuild. Prog. 51 (2, 3) (2004) 173–203.

[29] M. Greco, C. Lugni, Numerical study of parametric roll on a fishing vessel, ASME 2013 32nd International Conference on Ocean, Offshore and Arctic Engineering, American Society of Mechanical Engineers, 2013.

[30] I. Ghamari, O.M. Faltinsen, M. Greco, Investigation of parametric resonance in roll for container carrier ships, ASME 2015 34th International Conference on Ocean, Offshore and Arctic Engineering, American Society of Mechanical Engineers, 2015.

[31] I. Ghamari, O.M. Faltinsen, M. Greco, C. Lugni, Parametric resonance of a fishing vessel with and without anti-roll tank: an experimental and numerical study, ASME 2017 36th International Conference on Ocean, Offshore and Arctic Engineering, American Society of Mechanical Engineers, 2017.

[32] I. Ghamari, Numerical and Experimental Study on the Ship Parametric Roll Resonance and the Effect of Anti-Roll Tank, Norwegian University of Science and Technology (NTNU), 2019 Ph.D. thesis.

[33] M. Greco, B. Bouscasse, C. Lugni, 3-d seakeeping analysis with water on deck and slamming. Part 2: experiments and physical investigation, J. Fluids Struct. 33 (2012) 148–179.

[34] W. Cummins, The Impulse Response Function and Ship Motions, Technical Report, David Taylor Model Basin Washington DC, 1962.

[35] M. Greco, C. Lugni, O.M. Faltinsen, Can the water on deck influence the parametric roll of a FPSO? A numerical and experimental investigation, Eur. J. Mech.-B/Fluids 47 (2014) 188–201.

[36] J.S. Pawlowski, D.W. Bass, A theoretical and numerical model of ship motions in heavy seas, SNAME Trans. 99 (1991).

[37] M. Greco, C. Lugni, 3-d seakeeping analysis with water on deck and slamming. Part 1: numerical solver, J. Fluids Struct. 33 (2012) 127–147.

[38] M. Greco, C. Lugni, 3-d seakeeping analysis with water on deck and slamming. Part 1: numerical solver, J. Fluids Struct. 33 (2012) 127–147.

[39] K. Aarsæther, D. Kristiansen, B. Su, C. Lugni, Modelling of roll damping effects for a fishing vessel with forward speed, ASME 2015 34th International Conference on Ocean, Offshore and Arctic Engineering, American Society of Mechanical Engineers, 2015.

[40] O.M. Faltinsen, Hydrodynamics of High-Speed Marine Vehicles, Cambridge University press, 2005.

[41] N. Umeda, H. Hashimoto, D. Vassalos, S. Urano, K. Okou, Nonlinear dynamics on parametric roll resonance with realistic numerical modelling, Int. Shipbuild. Prog. 51 (2, 3) (2004) 205–220.

[42] H. Sadat-Hosseini, F. Stern, A. Olivieri, E.F. Campana, H. Hashimoto, N. Umeda, G. Bulian, A. Francescutto, Head-wave parametric rolling of a surface combatant, Ocean Eng. 37 (10) (2010) 859–878.